

Review paper: Virtual sources and their responses, Part I: time-reversal acoustics and seismic interferometry

Kees Wapenaar* and Jan Thorbecke

Department of Geoscience and Engineering, Delft University of Technology, PO Box 5048, 2600 GA Delft, The Netherlands

Received July 2016, revision accepted December 2016

ABSTRACT

A focusing acoustic wave field, emitted into a medium from its boundary, converges to a focal spot around the designated focal point. Subsequently, the focused field acts as a virtual source that emits a field propagating away from the focal point, mimicking the response to a real source at the position of the focal point. In this first part of a two-part review paper on virtual sources and their responses, we define the focusing wave field as the time reversal of an observed point-source response. This approach underlies time-reversal acoustics and seismic interferometry. We analyse the propagation of a time-reversed point-source response through an inhomogeneous medium, paying particular attention to the effect of internal multiples. We investigate the differences between emitting the focusing field from a closed boundary and from an open boundary, and we analyse in detail the properties of the virtual source. Whereas emitting the time-reversed field from a closed boundary yields an accurate isotropic virtual source, emitting the field from an open boundary leads to a highly directional virtual source and significant artefacts related to multiple scattering. The latter problems are addressed in Part II, where we define the focusing wave field as an inverse filter that accounts for primaries and multiples.

Key words: Virtual source, Green's function retrieval, Multiples.

INTRODUCTION

Motivation

The concept “virtual source” plays a role in a number of current acoustic and seismic methods, namely, time-reversal acoustics, seismic interferometry, and data-driven single-sided focusing. This two-part review paper discusses these methods in a unified way using the so-called “homogeneous Green's function” and its mathematical representations as the unifying elements. By discussing these methods together, their mutual relations and differences are made apparent. Time-reversal acoustics and seismic interferometry (discussed in Part I) are two sides of the same coin, with similar advantages and shortcomings. Data-driven single-sided focusing (discussed in Part II) circumvents several of the shortcomings. It underlies

a novel imaging method that accounts for internal multiples (so-called “Marchenko imaging”), and it provides a basis for improving time-reversal acoustics and seismic interferometry.

Virtual sources and their responses

A virtual acoustic or seismic source inside a medium can be created by emitting a focusing wave field from the boundary into the medium. A properly designed focusing wave field propagates through the medium and converges towards its designated focal point. Because, at the focal point, there is no sink to absorb the focused field, the field continues its propagation, diverging away from the focal point. This diverging wave field mimics the field that would be radiated by an actual source at the position of the focal point. In other words, the focal point acts as a virtual source. This principle has been known for a long time, and it has been used in different ways and in different fields. The most straightforward way to

*E-mail: c.p.a.wapenaar@tudelft.nl

focus a wave field inside a medium is by emitting the field by a curved transducer with a fixed focus. This is a well-known approach in ultrasonic imaging (Madsen, Goodsitt and Zagzebski 1981; Coulouvrat 1993). Another approach makes use of phased transducer arrays, the elements of which emit their signals with different time delays and amplitude factors, in such a way that all signals reach the focal point in-phase (Drinkwater and Wilcox 2006). The time delays can be varied, so the focal point (and, hence, the virtual-source position) is variable. Both approaches are a form of “physical focusing” because the focusing occurs in a physical experiment.

An alternative to physical focusing is “synthetic focusing”. When responses to individual point sources have been recorded, focusing can be carried out as a processing step after the actual acquisition. This is done by combining the point-source responses with appropriate time delays and amplitude factors. In ultrasonic imaging, this approach is known as the “synthetic aperture focusing technique” (Langenberg *et al.* 1986), whereas in seismic exploration, this is the standard way to “redatum” seismic sources from the acquisition surface into the subsurface (Berkhout 1984; Berryhill 1984; Esmersoy and Oristaglio 1988; Berkhout and Wapenaar 1993). Despite the differences in implementation, a virtual source created by synthetic focusing has the same properties as that created by a phased transducer array, steered with the same time delays and amplitude factors. This is a consequence of the linearity of the wave equation. Because, in seismic exploration, a physical phased array is impracticable, seismic virtual sources are created only synthetically, i.e., by redatuming.

These classical virtual-source approaches consider the focusing field as a relatively simple field that propagates directly from the acquisition surface to the focal point, without being scattered on its course. In most practical approaches, the focusing wave field is simply defined as the time reversal of the direct field of a source at the focal point, observed at the surface. This direct field is often modelled in a smoothed version of the actual medium, which is called the background medium in ultrasonics and is known as the macro velocity model in seismic exploration. The direct field may contain triplications related to caustics occurring during propagation through the smoothed medium, but it does not contain multiply scattered events related to the inhomogeneities of the actual medium. As a consequence, when the time reversal of the direct field is emitted into the actual medium (physically or synthetically), it will not only converge solely to the focal point but it will also create ghost foci. Hence, the created virtual source can, at best, be seen as an approximation of a real source. Another practical limitation is that the medium can often be accessed

from one side only. This implies that the focal point is also illuminated from one side only; hence, the created virtual source will be far from isotropic. For example, in the situation of seismic exploration, the medium can only be accessed from above; hence, the discussed classical approach leads to an approximate virtual source that radiates mainly downward and which is contaminated by scattering artefacts (see Figure 1).

In this two-part review paper, we discuss a number of wave-equation-based methodologies to create virtual sources in strongly inhomogeneous media and we compare the properties of these virtual sources and their responses. The first approach (discussed in Part I) is “time-reversal acoustics”, as advocated by Fink and co-workers (Fink 1997; Fink and Prada 2001). In the most basic form of time-reversal acoustics, the response to a source inside a medium is measured at its entire boundary, reversed in time, and physically emitted back into the medium by a phased transducer array along the entire boundary. Assuming that the medium is lossless, the time-reversed wave field obeys the same wave equation as the original wave field, but it propagates in the opposite direction. Hence, it focuses at zero time at the original source position. Subsequently, the focused field acts as an isotropic virtual source that radiates the same field as the original source into the medium. We also discuss the limitations when the time-reversed wave field can be emitted into the medium from only a part of its boundary.

The second approach (also discussed in Part I) is “seismic interferometry” (Bakulin and Calvert 2006; Gouédard *et al.* 2008; Schuster 2009; Snieder *et al.* 2009; Wapenaar *et al.* 2010). Suppose two physical receivers observe the responses to many uncorrelated sources that lie, for example, on a boundary enclosing the receivers. Then, the cross correlation of the responses at the two receivers converges to the response at one of the receivers as if there were a source at the position of the other. We review the analogy of this approach with time-reversal acoustics and, based on this analogy, discuss the limitations of the “interferometric virtual source” when the primary sources are present on only a part of the boundary enclosing the receivers.

The third approach (discussed in Part II) is “data-driven single-sided focusing”, which forms the basis for “Marchenko imaging” (Broggini and Snieder 2012; Wapenaar *et al.* 2014; van der Neut *et al.* 2015). This approach uses the reflection response measured at one side of a medium and an estimate of direct arrivals to focus at the position of a virtual source inside the medium and to retrieve the full response to this virtual source throughout the medium. Unlike in seismic interferometry, no physical receiver is needed at the position of the virtual

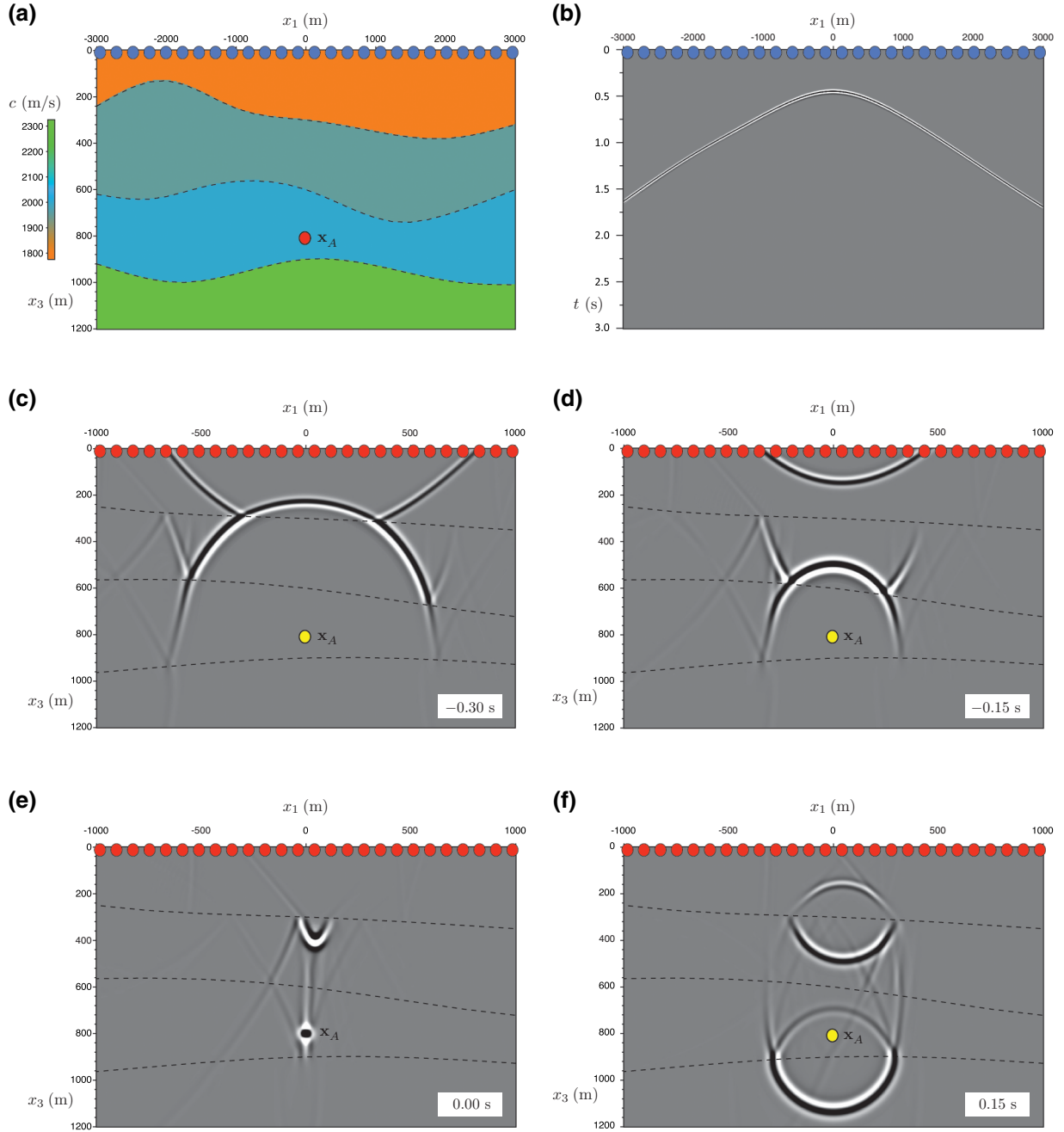


Figure 1 Illustration of the limitations of the classical virtual-source approach. (a) Inhomogeneous medium with absorbing boundary. (b) Modelled direct arrival at the upper boundary of the response to a source at the position of the designated focal point (the red dot at $\mathbf{x}_A = (0, 800)$ m in (a)). The source wavelet is a Ricker wavelet with a central frequency of 30 Hz. The time-reversal of this response is emitted into the medium from the upper boundary, serving as an approximation of the focusing wave field. (c) Focusing wave field at $t = -0.30$ s (prior to focusing). (d) Idem, at $t = -0.15$ s. (e) Focused wave field at $t = 0$ s. This represents the approximate virtual source for the field for $t > 0$. Note the smeared ghosts focus just below the first interface, besides the focal spot at \mathbf{x}_A . (f) Field at $t = 0.15$ s, which represents the approximate virtual-source response. Note that the virtual source radiates mainly downward.

source. Moreover, we will show that the virtual source created by the Marchenko method has comparable isotropic radiation properties as that obtained with ideal (omnidirectional) time-reversal acoustics despite the fact that the reflection response used in the Marchenko method is measured at one side of the medium only.

TIME-REVERSAL ACOUSTICS

Theory of time-reversal acoustics

We review the principle of time-reversal acoustics in its basic form. Consider an arbitrary inhomogeneous lossless acoustic medium, in which a source is placed at $\mathbf{x} = \mathbf{x}_A$ (Fig. 2a). Here, \mathbf{x} is the Cartesian coordinate vector $\mathbf{x} = (x_1, x_2, x_3)$; hence, $\mathbf{x}_A = (x_{1,A}, x_{2,A}, x_{3,A})$ (the positive x_3 -axis is pointing downward throughout this paper). The response to this source for an impulse at $t = 0$ is given by the Green's function $G(\mathbf{x}, \mathbf{x}_A, t)$, where \mathbf{x} is an arbitrary observation point and t denotes time. Receivers are placed on a boundary enclosing the source. These receivers record the Green's function $G(\mathbf{x}, \mathbf{x}_A, t)$ as a function of time for \mathbf{x} at the closed boundary. In a time-reversal experiment, the receivers are replaced by sources, and these sources emit the time-reversed Green's function $G(\mathbf{x}, \mathbf{x}_A, -t)$ from all \mathbf{x} at the closed boundary back into the medium (Fig. 2b). Because, for a lossless medium, the wave equation is symmetric in time (it contains only even-order time derivatives), the time-reversed Green's function obeys the same wave equation as the original Green's function. Hence, the time-reversed field emitted from the boundary into the medium follows the same paths as the original field, but in opposite direction, and focuses at $t = 0$ at the original source position \mathbf{x}_A . Note that this holds true for any inhomogeneous medium as long as the medium is lossless. McMechan (1982) exploited this property in a method to determine the source parameters, whereas Hemon (1978), Whitmore (1983), and McMechan (1983) used it as the basis for reverse-time migration.

In a time-reversal experiment, the wave field at an arbitrary location \mathbf{x}_B in the medium is described by

$$u(\mathbf{x}_B, t) \propto \oint_{\partial\mathbb{D}} \underbrace{G(\mathbf{x}_B, \mathbf{x}, t)}_{\text{"propagator"}} * \underbrace{G(\mathbf{x}, \mathbf{x}_A, -t)}_{\text{"source"}} d^2\mathbf{x}, \quad (1)$$

where $*$ denotes convolution, \propto denotes "proportional to", and $\partial\mathbb{D}$ represents the closed boundary. In this equation, the time-reversed Green's function $G(\mathbf{x}, \mathbf{x}_A, -t)$ acts as a source at \mathbf{x} on $\partial\mathbb{D}$, whereas $G(\mathbf{x}_B, \mathbf{x}, t)$ propagates its response from \mathbf{x} to \mathbf{x}_B . According to the superposition principle, the total

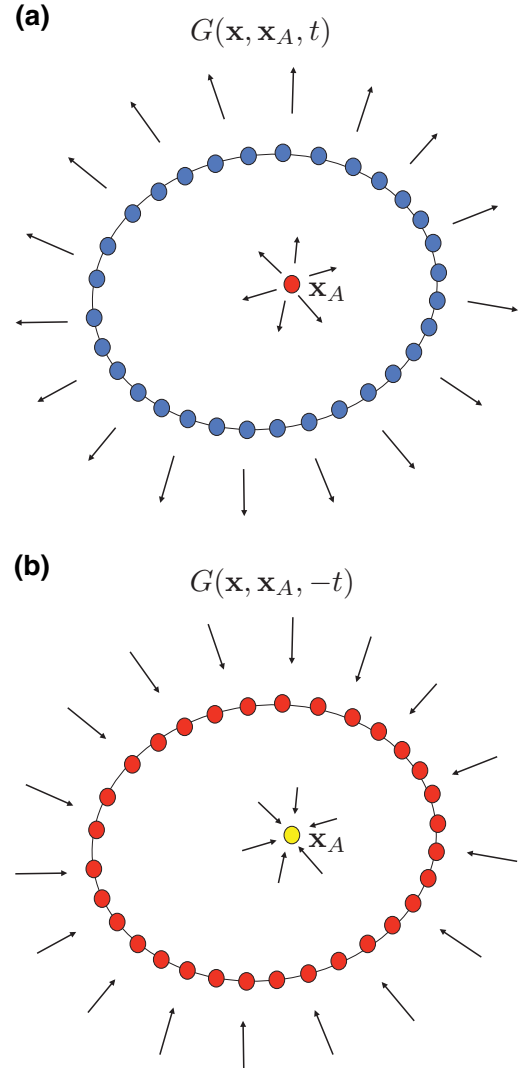


Figure 2 Principle of time-reversal acoustics (Fink 1997). (a) The Green's function $G(\mathbf{x}, \mathbf{x}_A, t)$ represents the impulse response to a source at \mathbf{x}_A , observed at \mathbf{x} . The Green's function is recorded by receivers on a boundary enclosing the source. (b) The time-reversed Green's function $G(\mathbf{x}, \mathbf{x}_A, -t)$ is emitted from all \mathbf{x} at the boundary into the medium and focuses at \mathbf{x}_A .

response at \mathbf{x}_B is the sum of the responses to all sources on $\partial\mathbb{D}$, which is taken care of by the integral in equation (1). The field $u(\mathbf{x}_B, t)$ focuses at $\mathbf{x}_B = \mathbf{x}_A$ at $t = 0$. Because there is no sink at this point to absorb the energy of the focused field, the field $u(\mathbf{x}_B, t)$ for arbitrary \mathbf{x}_B and $t > 0$ can be seen as the response to a virtual source at \mathbf{x}_A at $t = 0$, hence $G(\mathbf{x}_B, \mathbf{x}_A, t)$. Note, however, that $u(\mathbf{x}_B, t)$ consists of a causal and an acausal part according to

$$u(\mathbf{x}_B, t) = G(\mathbf{x}_B, \mathbf{x}_A, t) + G(\mathbf{x}_B, \mathbf{x}_A, -t), \quad (2)$$

where the acausal part $G(\mathbf{x}_B, \mathbf{x}_A, -t)$ represents the field propagating back from the time-reversed sources at $\partial\mathbb{D}$, prior to focusing at \mathbf{x}_A at $t = 0$. Combining equations (1) and (2) yields

$$G_h(\mathbf{x}_B, \mathbf{x}_A, t) \propto \oint_{\partial\mathbb{D}} G(\mathbf{x}_B, \mathbf{x}, t) * G(\mathbf{x}, \mathbf{x}_A, -t) d^2\mathbf{x}, \quad (3)$$

where $G_h(\mathbf{x}_B, \mathbf{x}_A, t)$ stands for the homogeneous Green's function defined as

$$G_h(\mathbf{x}_B, \mathbf{x}_A, t) = G(\mathbf{x}_B, \mathbf{x}_A, t) + G(\mathbf{x}_B, \mathbf{x}_A, -t). \quad (4)$$

The intuitive derivation presented here, which is due to Derode *et al.* (2003a,b), explains what happens in a time-reversal experiment. Note that $G_h(\mathbf{x}, \mathbf{x}_A, t)$ obeys a wave equation without a source at the right-hand side (equation (A-11), a homogeneous differential equation), hence the name homogeneous Green's function. In Appendix A, we derive equation (3), the homogeneous Green's function representation, in a more fundamental way. Starting with an exact representation (equation A-20), we arrive at equation (3) after a number of approximations. Moreover, we find a proportionality factor of $2/\rho_0 c_0$, where ρ_0 and c_0 are the mass density and the propagation velocity of the homogeneous medium outside $\partial\mathbb{D}$. From the derivation in Appendix A, it also follows that the integral in equation (3) needs not be evaluated over those parts of $\partial\mathbb{D}$ that are either free (where the pressure vanishes) or fixed (where the normal component of the particle velocity vanishes). In the following, we assume that no parts of $\partial\mathbb{D}$ are free or fixed so that the integral in equation (3) needs to be evaluated along the entire closed boundary $\partial\mathbb{D}$.

In Appendix A, we introduce a second type of Green's function $\mathcal{G}(\mathbf{x}, \mathbf{x}_A, t)$, which is related to $G(\mathbf{x}, \mathbf{x}_A, t)$ via

$$G(\mathbf{x}, \mathbf{x}_A, t) = \frac{\partial \mathcal{G}(\mathbf{x}, \mathbf{x}_A, t)}{\partial t}. \quad (5)$$

Analogous to equations (3) and (4), the representation for the homogeneous Green's function $\mathcal{G}_h(\mathbf{x}_B, \mathbf{x}_A, t)$ reads

$$\mathcal{G}_h(\mathbf{x}_B, \mathbf{x}_A, t) \propto -\frac{\partial}{\partial t} \oint_{\partial\mathbb{D}} \mathcal{G}(\mathbf{x}_B, \mathbf{x}, t) * \mathcal{G}(\mathbf{x}, \mathbf{x}_A, -t) d^2\mathbf{x}, \quad (6)$$

with

$$\mathcal{G}_h(\mathbf{x}_B, \mathbf{x}_A, t) = \mathcal{G}(\mathbf{x}_B, \mathbf{x}_A, t) - \mathcal{G}(\mathbf{x}_B, \mathbf{x}_A, -t). \quad (7)$$

Both forms of the Green's function appear in the literature on time-reversal acoustics, which is why we give both representations. Note that $G(\mathbf{x}, \mathbf{x}_A, t)$ has a clear physical meaning, i.e., acoustic pressure observed at \mathbf{x} in response to an impulsive source of volume-injection rate density at \mathbf{x}_A , i.e., $q(\mathbf{x}, t) = \delta(\mathbf{x} - \mathbf{x}_A)\delta(t)$; see equations (A-1)–(A-5) in Appendix A.

Suppose that the source at \mathbf{x}_A is not an impulse but is characterised by a time-dependent source wavelet $s(t)$, i.e., $q(\mathbf{x}, t) = \delta(\mathbf{x} - \mathbf{x}_A)s(t)$. Then, the acoustic pressure field at \mathbf{x} is given by $p(\mathbf{x}, \mathbf{x}_A, t) = G(\mathbf{x}, \mathbf{x}_A, t) * s(t)$. In a time-reversal experiment, $p(\mathbf{x}, \mathbf{x}_A, -t)$ is emitted from the closed boundary back into the medium. By convolving both sides of equation (3) with $s(-t)$ and inserting the factor $2/\rho_0 c_0$, we obtain

$$G_h(\mathbf{x}_B, \mathbf{x}_A, t) * s(-t) \approx \frac{2}{\rho_0 c_0} \oint_{\partial\mathbb{D}} G(\mathbf{x}_B, \mathbf{x}, t) * p(\mathbf{x}, \mathbf{x}_A, -t) d^2\mathbf{x}. \quad (8)$$

Alternatively, when we replace $p/\rho_0 c_0$ by the normal component of the particle velocity v_n , we obtain

$$G_h(\mathbf{x}_B, \mathbf{x}_A, t) * s(-t) \approx 2 \oint_{\partial\mathbb{D}} G(\mathbf{x}_B, \mathbf{x}, t) * v_n(\mathbf{x}, \mathbf{x}_A, -t) d^2\mathbf{x}. \quad (9)$$

Although expressions (8) and (9) are similar, from the more fundamental derivation in Appendix A, it follows that equation (9) is more accurate than equation (8) (and, hence, also more accurate than equation (3)). The underlying assumptions for equation (9) are that the medium outside $\partial\mathbb{D}$ is homogeneous and that evanescent waves on $\partial\mathbb{D}$ are negligible. Equation (8) holds under the additional assumption that $\partial\mathbb{D}$ is a sphere with a very large radius.

Numerical examples

We illustrate equation (9) with two 2D numerical examples. In 2D, the Cartesian coordinate vector is replaced by $\mathbf{x} = (x_1, x_3)$, and boundary integrals like those in equations (8) and (9) become line integrals. For convenience, we keep calling $\partial\mathbb{D}$ a boundary. For the configuration of Fig. 1(a), Fig. 3(a) shows the response $v_n(\mathbf{x}, \mathbf{x}_A, t)$ to a source at $\mathbf{x}_A = (0, 800)$ m, observed by velocity receivers at all \mathbf{x} on the enclosing boundary. The source wavelet is a Ricker wavelet with a central frequency of 30 Hz. Following equation (9), the time reversal of this response is emitted from the enclosing boundary into the medium and propagates to all \mathbf{x}_B in the medium. Snapshots of $G_h(\mathbf{x}_B, \mathbf{x}_A, t) * s(-t)$ (fixed \mathbf{x}_A , variable \mathbf{x}_B) are shown in Fig. 3(b), (c), (d), and (e) for $t = -0.30$ seconds, $t = -0.15$ seconds, $t = 0.0$ second and $t = 0.15$ seconds, respectively. Note that, for $t < 0$ (Fig. 3(b) and (c)), the field $G_h(\mathbf{x}_B, \mathbf{x}_A, t) * s(-t)$ is a focusing field propagating toward \mathbf{x}_A . After an intricate interplay of up- and downward propagating primary and multiply-reflected waves, the field is focused at $t = 0$ onto a small region around \mathbf{x}_A (Fig. 3(d)). This is the focal spot, which is analysed in the next section. The focused

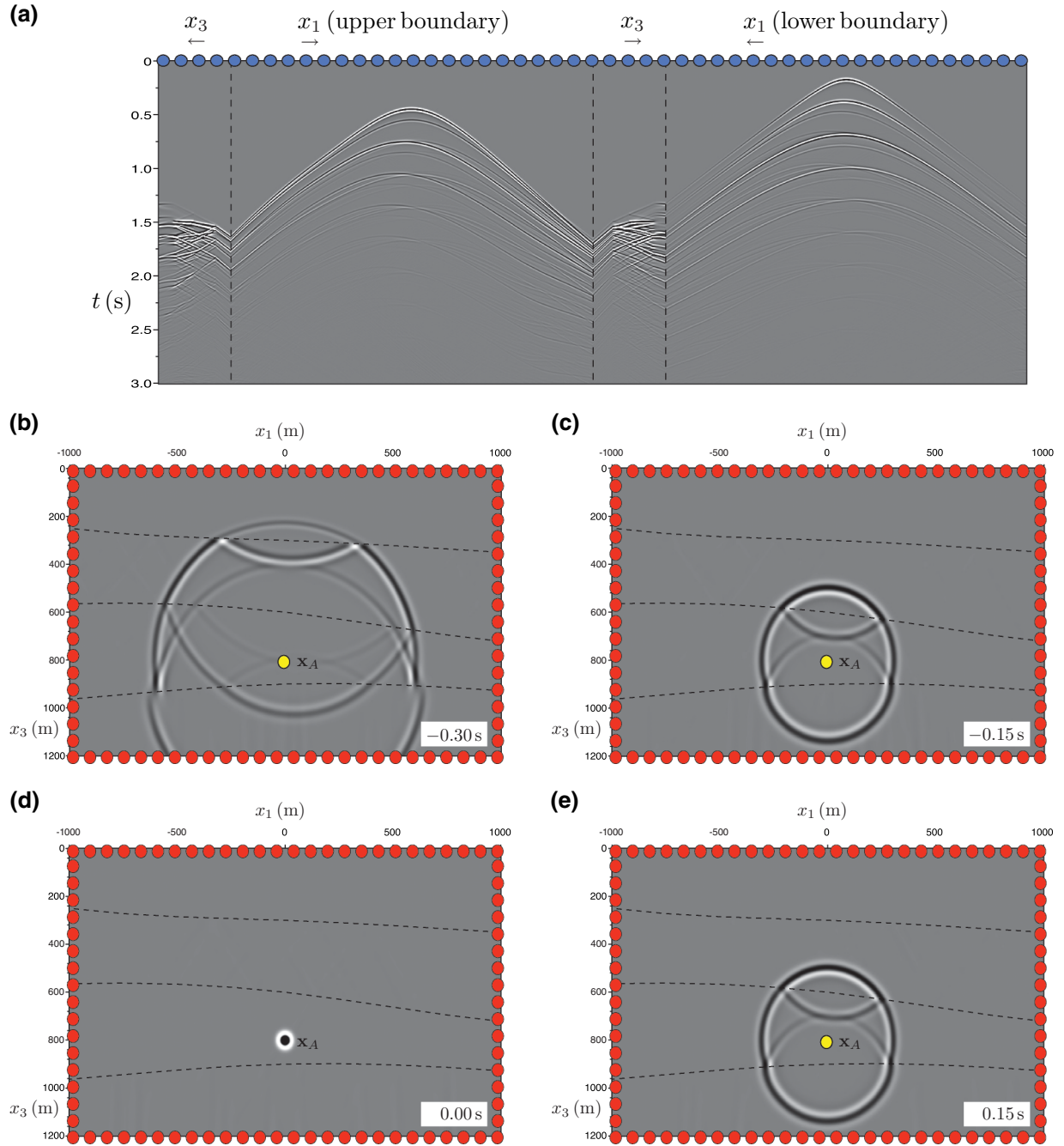


Figure 3 Illustration of a time-reversal experiment for the 2D inhomogeneous medium of Fig. 1. (a) Modelled response $v_n(\mathbf{x}, \mathbf{x}_A, t)$ at the enclosing boundary, with $\mathbf{x}_A = (0, 800)$ m indicated by the red dot in Fig. 1(a). The source wavelet is a Ricker wavelet with a central frequency of 30 Hz. The time reversal of this response is emitted into the medium from the entire enclosing boundary. (b) Focusing wave field $G_h(\mathbf{x}_B, \mathbf{x}_A, t) * s(-t)$ (for variable \mathbf{x}_B) at $t = -0.30$ seconds (prior to focusing). (c) Idem, at $t = -0.15$ seconds. (d) Focused wave field $G_h(\mathbf{x}_B, \mathbf{x}_A, t) * s(-t)$ at $t = 0$ s. This focal spot represents the virtual source for the field for $t > 0$. (e) Field $G_h(\mathbf{x}_B, \mathbf{x}_A, t) * s(-t)$ at $t = 0.15$ s, which represents the virtual-source response. Note the isotropic character of the virtual source.

field acts as a virtual source for the field for $t > 0$ (Fig. 3(e)). Note that this virtual source acts as a perfect omnidirectional monopole source.

The perfect recovery of the virtual-source response in Fig. 3 could only be achieved because the medium was accessible from all sides. Suppose $v_n(\mathbf{x}, \mathbf{x}_A, t)$ is only recorded at the upper boundary. Emitting the time reversal of this response from the upper boundary into the medium results in the wave field shown in Fig. 4. Note that the focused wave field at $t = 0$ in Fig. 4(c) exhibits even more ghost foci than the focused direct wave at $t = 0$ in Fig. 1(e). Moreover, similar as in Fig. 1, the approximate virtual source at \mathbf{x}_A radiates mainly downward.

The second example (Fig. 4) shows that the time-reversal approach does not properly account for multiple scattering when the medium is accessible from one side only. This seems contradictory to the conventional wisdom that the time-reversal method not only accounts for multiple scattering but even benefits from it by achieving higher spatial resolution. An experiment discussed by Fink (1997) indeed demonstrates that the spatial resolution improves by emitting a time-reversed field through a highly scattering medium, in comparison with sending it through a homogeneous medium (also in that experiment, the time-reversed field is emitted from one side only into the medium). The character of the inhomogeneous medium in Fink's experiment, however, is very different from that of the medium in Fig. 1(a). The inhomogeneous medium in Fink's experiment consists of many randomly placed point-like scatterers (actually, line scatterers in 3D), which effectively widen the aperture angle (mainly through forward multiple scattering), thus improving the resolution. More recent experiments have shown that this can even lead to resolution beyond the diffraction limit (Lerosey *et al.* 2007). In contrast, the inhomogeneous medium in Fig. 1(a) consists of layers with different propagation velocities and mass densities, separated by curved interfaces. In this type of configuration, which better represents the geology of the Earth's subsurface, backward multiple scattering (down-up-down-up...) is much more prominent than forward multiple scattering (down-down-down... or up-up-up...). Here, the single-sided time-reversal approach breaks down because the intricate interplay of up- and downward propagating primary and multiply-reflected waves, which led to the near-perfect focus in Fig. 3(d), requires illumination from all sides (at least from above and from below). Model-driven source characterisation (McMechan 1982) and reverse-time migration (Whitmore 1983; McMechan 1983) suffer from the same limitations: even when the medium (through which the

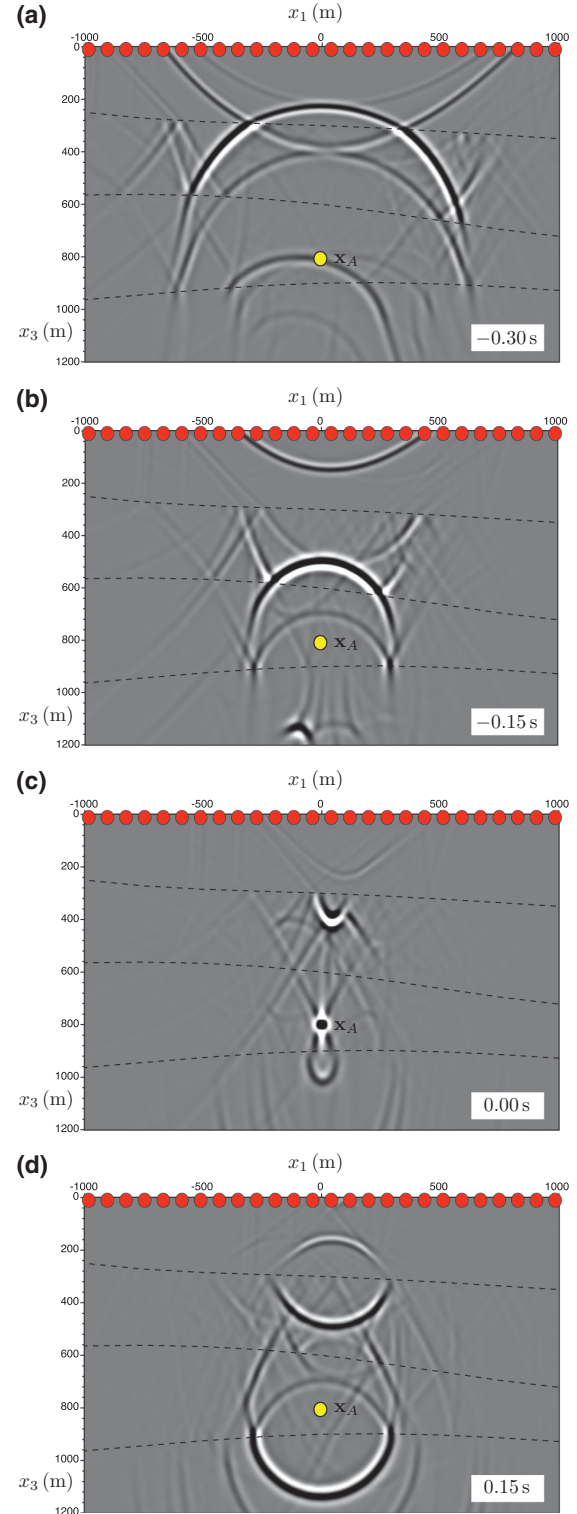


Figure 4 Illustration of the limitations of the time-reversal approach when the medium is accessible from one side only. Here, the time reversal of $v_n(\mathbf{x}, \mathbf{x}_A, t)$ is emitted only from the upper boundary into the medium.

time-reversed field is propagated numerically) would be perfectly known, backward multiply-scattered waves would lead to artefacts like those in Fig. 4. The Marchenko method, which is discussed in Part II, is particularly suited to account for backward multiply-scattered waves. It leads to accurate virtual-source responses like that in Fig. 3 even when the medium is accessible from one side only.

Analysis of the focal spot (=the virtual source)

The focal spot of a time-reversal experiment is defined as the space- and time-dependent field, evaluated at $t = 0$. The focal spots in Figs. 1(e), 3(d), and 4(c) are shown in Fig. 5(a), (b), and (c). These figures show the amplitudes as a function of $\mathbf{x} = (x_1, x_3)$, with the maximum amplitudes scaled to 1. In the ideal case, the focal spot follows from the left-hand side of equation (9); hence

$$V(\mathbf{x}, \mathbf{x}_A) = [G_h(\mathbf{x}, \mathbf{x}_A, t) * s(-t)]_{t=0} \quad (10)$$

(for convenience, we replaced \mathbf{x}_B by \mathbf{x}). Equation (10) is the basis for the quantification of the finite spatial resolution of the focus obtained with a time-reversal experiment in a medium that is accessible from all sides (as in Figs. 3(d) and 5(b)).

The focal spot can be interpreted as the virtual source of the field for $t > 0$. Note that, unlike a real point source, which is defined by a spatial delta function in the right-hand side of the wave equation, i.e.,

$$q(\mathbf{x}, t) = \delta(\mathbf{x} - \mathbf{x}_A)s(t), \quad (11)$$

the virtual source is smeared out in space, as quantified by equation (10). The virtual-source function $V(\mathbf{x}, \mathbf{x}_A)$ can be interpreted as an initial condition at $t = 0$ for the field $G_h(\mathbf{x}, \mathbf{x}_A, t) * s(-t)$ for $t > 0$ (which is not singular; see equation (A-11) in Appendix A). Since the wave equation is second order in time, a second initial condition is required to define the field for $t > 0$ uniquely. Therefore, we also consider the following function:

$$\dot{V}(\mathbf{x}, \mathbf{x}_A) = \left[\frac{\partial}{\partial t} \{G_h(\mathbf{x}, \mathbf{x}_A, t) * s(-t)\} \right]_{t=0}. \quad (12)$$

The functions $V(\mathbf{x}, \mathbf{x}_A)$ and $\dot{V}(\mathbf{x}, \mathbf{x}_A)$ together define the virtual source for the field for $t > 0$ in terms of its initial conditions at $t = 0$.

The question now arises how the finite resolution of the virtual-source function at $t = 0$ affects the field for $t > 0$. This

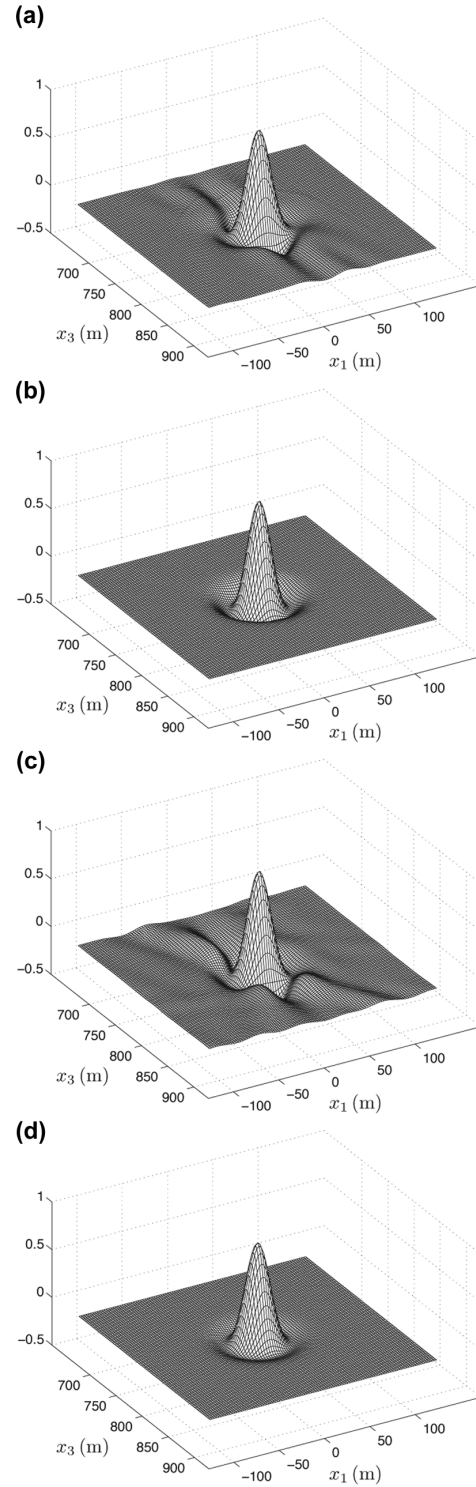


Figure 5 (a) Amplitudes as a function of $\mathbf{x} = (x_1, x_3)$ of the focal spot at $t = 0$ in Fig. 1(e). A focal spot at $t = 0$ is the virtual-source of the field for $t > 0$. (b) *Idem*, for the focal spot (=virtual source) in Fig. 3(d). (c) *Idem*, for the focal spot (=virtual source) in Fig. 4(c). (d) Analytically derived virtual-source function for the 3D situation (equation (16)).

field is given by equation (9) or, using the definition of the homogeneous Green's function (equation (4)), by

$$\{G(\mathbf{x}, \mathbf{x}_A, t) + G(\mathbf{x}, \mathbf{x}_A, -t)\} * s(-t). \quad (13)$$

Suppose $s(t)$ is a source wavelet that is non-zero between $t = -t_s$ and $t = t_s$. Then, the two terms in equation (13) overlap each other between $t = -t_s$ and $t = t_s$, but outside this time interval, they are separable. Hence, for $t > t_s$, the response to the virtual source is given by $G(\mathbf{x}, \mathbf{x}_A, t) * s(-t)$, which is identical to the response to a point source, i.e., $q(\mathbf{x}, t) = \delta(\mathbf{x} - \mathbf{x}_A)s(-t)$, even though the virtual-source functions $V(\mathbf{x}, \mathbf{x}_A)$ and $\dot{V}(\mathbf{x}, \mathbf{x}_A)$ are smeared out in space. Only for $t \leq t_s$ is the field of the virtual source different from that of a point source.

Next, we consider analytical expressions for the virtual-source functions $V(\mathbf{x}, \mathbf{x}_A)$ and $\dot{V}(\mathbf{x}, \mathbf{x}_A)$. A more detailed analysis, for different types of source mechanisms and for elastodynamic waves, is given by Douma and Snieder (2015). Equations (10) and (12) can be analytically evaluated if we assume a homogeneous region in the neighbourhood of the virtual-source position \mathbf{x}_A , with propagation velocity \bar{c} and mass density $\bar{\rho}$. In Appendix B, we derive for the 3D situation

$$V_{3D}(\mathbf{x}, \mathbf{x}_A) = -\frac{\bar{\rho}}{4\pi r} \{\dot{s}(r/\bar{c}) - \dot{s}(-r/\bar{c})\}, \quad (14)$$

$$\dot{V}_{3D}(\mathbf{x}, \mathbf{x}_A) = \frac{\bar{\rho}}{4\pi r} \{\ddot{s}(r/\bar{c}) - \ddot{s}(-r/\bar{c})\}, \quad (15)$$

where $r = |\mathbf{x} - \mathbf{x}_A|$ and $\dot{s}(t)$ and $\ddot{s}(t)$ denote the first- and second-order derivatives, respectively, of the source wavelet $s(t)$. The limits for $\mathbf{x} \rightarrow \mathbf{x}_A$ are finite and are given by equations (B-6) and (B-8). Note that, for a symmetric source wavelet $s_{\text{sym}}(t) = s_{\text{sym}}(-t)$, expressions (14) and (15) simplify to

$$V_{3D}(\mathbf{x}, \mathbf{x}_A) = -\frac{\bar{\rho}}{2\pi r} \dot{s}_{\text{sym}}(r/\bar{c}), \quad (16)$$

$$\dot{V}_{3D}(\mathbf{x}, \mathbf{x}_A) = 0. \quad (17)$$

For an anti-symmetric source wavelet $s_{\text{asym}}(t) = -s_{\text{asym}}(-t)$, equations (14) and (15) become

$$V_{3D}(\mathbf{x}, \mathbf{x}_A) = 0, \quad (18)$$

$$\dot{V}_{3D}(\mathbf{x}, \mathbf{x}_A) = \frac{\bar{\rho}}{2\pi r} \dot{s}_{\text{asym}}(r/\bar{c}). \quad (19)$$

Note that, in this case, the virtual-source function $V_{3D}(\mathbf{x}, \mathbf{x}_A)$ vanishes. Because, in a time-reversal experiment, one usually does not consider the derivative of the wave field, a symmetric source wavelet is preferred over an anti-symmetric one because it yields a non-zero focal spot (equation (16)).

A Ricker wavelet is an example of a symmetric wavelet. Figure 5(d) shows a cross section in the (x_1, x_3) -plane of $V_{3D}(\mathbf{x}, \mathbf{x}_A)$, defined by equation (16), for a Ricker wavelet with a central frequency of 30 Hz, with $\bar{c} = 2000$ m/s and $\bar{\rho} = 1400$ kg/m³ (being the parameters of the layer in Fig. 1(a) that contains \mathbf{x}_A). Note that this analytically derived function exhibits a similar behaviour as the numerically obtained result in Fig. 5(b), although the side lobes of the function in Fig. 5(d) are less strong. The difference is explained by the fact that Fig. 5(b) is the result of a 2D experiment, whereas Fig. 5(d) is a cross section of a 3D virtual-source function. Next, we analyse 2D and 1D virtual-source functions.

For the 2D situation, the virtual-source functions $V_{2D}(\mathbf{x}, \mathbf{x}_A)$ and $\dot{V}_{2D}(\mathbf{x}, \mathbf{x}_A)$ are given by equations (B-10) and (B-11). For a symmetric source wavelet $s_{\text{sym}}(t)$, these expressions are simplified to

$$V_{2D}(\mathbf{x}, \mathbf{x}_A) = -\frac{\bar{\rho}}{\pi} \int_{r/\bar{c}}^{\infty} \frac{\dot{s}_{\text{sym}}(t)}{\sqrt{t^2 - r^2/\bar{c}^2}} dt, \quad (20)$$

$$\dot{V}_{2D}(\mathbf{x}, \mathbf{x}_A) = 0. \quad (21)$$

For an anti-symmetric source wavelet $s_{\text{asym}}(t)$, these equations become

$$V_{2D}(\mathbf{x}, \mathbf{x}_A) = 0, \quad (22)$$

$$\dot{V}_{2D}(\mathbf{x}, \mathbf{x}_A) = \frac{\bar{\rho}}{\pi} \int_{r/\bar{c}}^{\infty} \frac{\dot{s}_{\text{asym}}(t)}{\sqrt{t^2 - r^2/\bar{c}^2}} dt. \quad (23)$$

For the 1D situation, the virtual-source functions are given by equations (B-13) and (B-14). For a symmetric source wavelet $s_{\text{sym}}(t)$, these expressions are simplified to

$$V_{1D}(x_3, x_{3,A}) = \bar{\rho} \bar{c} s_{\text{sym}}(r/\bar{c}), \quad (24)$$

$$\dot{V}_{1D}(x_3, x_{3,A}) = 0, \quad (25)$$

where $r = |x_3 - x_{3,A}|$. For an anti-symmetric source wavelet $s_{\text{asym}}(t)$, we obtain

$$V_{1D}(x_3, x_{3,A}) = 0, \quad (26)$$

$$\dot{V}_{1D}(x_3, x_{3,A}) = -\bar{\rho} \bar{c} \dot{s}_{\text{asym}}(r/\bar{c}). \quad (27)$$

Hence, also for the 2D and 1D situations, a symmetric source wavelet is preferred over an anti-symmetric one. For a Ricker wavelet with a central frequency of 30 Hz, equation (20) describes the virtual-source function in Fig. 5(b). Vertical cross sections along the x_3 -axis of $V_{3D}(\mathbf{x}, \mathbf{x}_A)$ (equation 16), $V_{2D}(\mathbf{x}, \mathbf{x}_A)$ (equation 20) and $V_{1D}(x_3, x_{3,A})$ (equation (24)) are shown in Fig. 6(a), (b), and (c). A comparison of these three virtual-source functions is shown in Fig. 6(d) (3D: solid line;

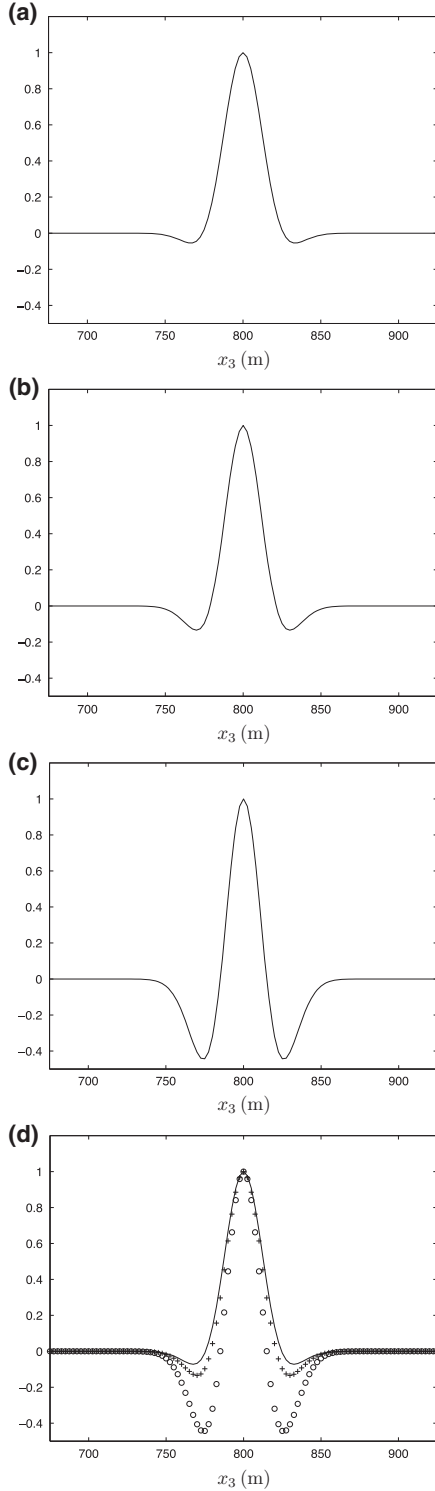


Figure 6 (a) Cross-section along the x_3 -axis of the 3D virtual-source function (equation (16) and Fig. 5(d)). (b) *Idem*, 2D virtual-source function (equation (20)). (c) *Idem*, 1D virtual-source function (equation (24)). (d) Comparison of the three virtual-source functions (solid line: 3D, pluses: 2D, circles: 1D).

2D: + symbols; 1D: o symbols). Note that the side lobes become stronger when the number of dimensions decreases, whereas the widths of the main lobes slightly decrease.

Finally, analogous to equations (10) and (12), we define virtual-source functions related to the second type of homogeneous Green's function $\mathcal{G}_h(\mathbf{x}, \mathbf{x}_A, t)$ according to

$$\mathcal{V}(\mathbf{x}, \mathbf{x}_A) = [\mathcal{G}_h(\mathbf{x}, \mathbf{x}_A, t) * s(-t)]_{t=0}, \quad (28)$$

$$\dot{\mathcal{V}}(\mathbf{x}, \mathbf{x}_A) = \left[\frac{\partial}{\partial t} \{ \mathcal{G}_h(\mathbf{x}, \mathbf{x}_A, t) * s(-t) \} \right]_{t=0}. \quad (29)$$

In Appendix B, we obtain for the 3D situation

$$\mathcal{V}_{3D}(\mathbf{x}, \mathbf{x}_A) = \frac{\bar{\rho}}{4\pi r} \{ s(r/\bar{c}) - s(-r/\bar{c}) \}, \quad (30)$$

$$\dot{\mathcal{V}}_{3D}(\mathbf{x}, \mathbf{x}_A) = -\frac{\bar{\rho}}{4\pi r} \{ \dot{s}(r/\bar{c}) - \dot{s}(-r/\bar{c}) \}, \quad (31)$$

with the limits for $\mathbf{x} \rightarrow \mathbf{x}_A$ given by equations (B-18) and (B-20). For a symmetric source wavelet $s_{\text{sym}}(t)$, expressions (30) and (31) are simplified to

$$\mathcal{V}_{3D}(\mathbf{x}, \mathbf{x}_A) = 0, \quad (32)$$

$$\dot{\mathcal{V}}_{3D}(\mathbf{x}, \mathbf{x}_A) = -\frac{\bar{\rho}}{2\pi r} \dot{s}_{\text{sym}}(r/\bar{c}) \quad (33)$$

and for an anti-symmetric source wavelet $s_{\text{asym}}(t)$, they become

$$\mathcal{V}_{3D}(\mathbf{x}, \mathbf{x}_A) = \frac{\bar{\rho}}{2\pi r} s_{\text{asym}}(r/\bar{c}), \quad (34)$$

$$\dot{\mathcal{V}}_{3D}(\mathbf{x}, \mathbf{x}_A) = 0. \quad (35)$$

Hence, in this case, an anti-symmetric source wavelet is preferred over a symmetric one. The same conclusion applies to the 2D and 1D situations.

This analysis shows that the type of wavelet has a significant influence on the virtual-source functions (or focal spots). This should be taken into account in the design of physical time-reversal experiments and in model-driven source characterisation and imaging algorithms.

SEISMIC INTERFEROMETRY

Theory of seismic interferometry

The basic principle of seismic interferometry can be best introduced by considering a slightly modified version of the homogeneous Green's function representation of equation (3). Applying source–receiver reciprocity to the second Green's function under the integral, we obtain

$$G_h(\mathbf{x}_B, \mathbf{x}_A, t) \approx \frac{2}{\rho_0 c_0} \oint_{\partial\mathbb{D}} G(\mathbf{x}_B, \mathbf{x}, t) * G(\mathbf{x}_A, \mathbf{x}, -t) d^2\mathbf{x}, \quad (36)$$

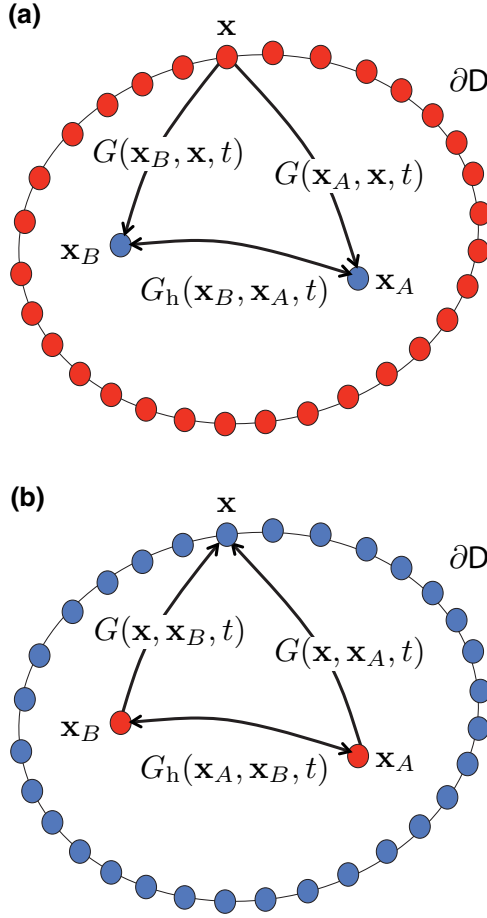


Figure 7 (a) Principle of seismic interferometry (Wapenaar *et al.* 2005). The Green's functions $G(\mathbf{x}_A, \mathbf{x}, t)$ and $G(\mathbf{x}_B, \mathbf{x}, t)$ represent the responses to a source at \mathbf{x} , observed at \mathbf{x}_A and \mathbf{x}_B , respectively. By cross correlating these responses and integrating over all sources on a closed boundary (equation (36)), the homogeneous Green's function $G_h(\mathbf{x}_B, \mathbf{x}_A, t)$ is retrieved. This is interpreted as the response to a virtual source at \mathbf{x}_A , observed by a receiver at \mathbf{x}_B , plus its time reversal. (b) By interchanging the roles of sources and receivers (Curtis *et al.* 2009), we retrieve $G_h(\mathbf{x}_A, \mathbf{x}_B, t)$, which is now interpreted as the response to a source at \mathbf{x}_B , observed by a virtual receiver at \mathbf{x}_A , plus its time reversal.

(Derode *et al.* 2003b; Wapenaar *et al.* 2002; Wapenaar, Fokkema and Snieder 2005; van Manen, Robertsson and Curtis 2005) see Fig. 7(a). The integrand represents the cross correlation of observations at \mathbf{x}_A and \mathbf{x}_B of responses to one and the same source at \mathbf{x} . The integration takes place along sources on a boundary $\partial\mathbb{D}$ enclosing the receivers at \mathbf{x}_A and \mathbf{x}_B . This yields the Green's function plus its time-reversed function (i.e., the homogeneous Green's function) for a source at the position of one of the receivers (at \mathbf{x}_A), observed at the position of the other (at \mathbf{x}_B). Because there is no real source at \mathbf{x}_A , the

retrieved Green's function is often called the virtual-source response (Schuster 2001; Bakulin and Calvert 2006). For the Green's function \mathcal{G} , introduced in equation (5), equation (36) becomes

$$\mathcal{G}_h(\mathbf{x}_B, \mathbf{x}_A, t) \approx -\frac{2}{\rho_0 c_0} \frac{\partial}{\partial t} \oint_{\partial\mathbb{D}} \mathcal{G}(\mathbf{x}_B, \mathbf{x}, t) * \mathcal{G}(\mathbf{x}_A, \mathbf{x}, -t) d^2\mathbf{x}. \quad (37)$$

Note that, when the roles of the sources and receivers are interchanged in equations (36) and (37), then \mathbf{x}_A and \mathbf{x}_B represent sources (see Fig. 7(b)), the integration takes place along receivers on $\partial\mathbb{D}$, and the retrieved Green's function represents an observation by a virtual receiver at the position of one of the sources (Curtis *et al.* 2009).

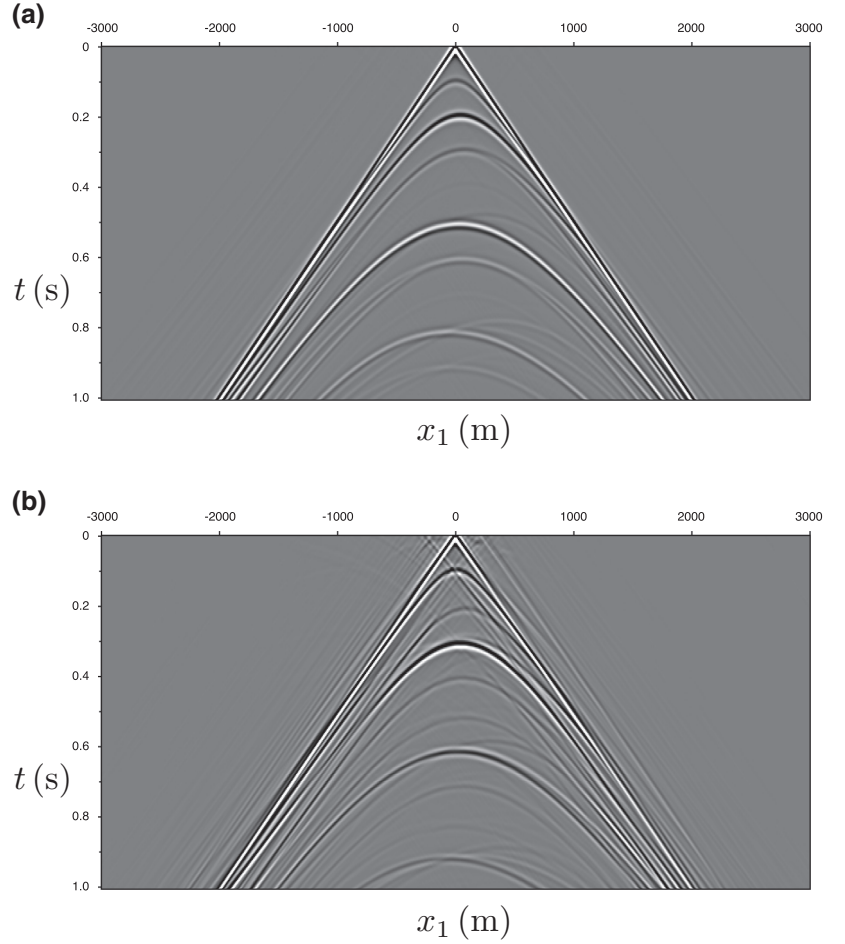
We return to the original situation, with sources and receivers as indicated in Fig. 7(a). When the sources at \mathbf{x} have a time-dependent source wavelet $s(t)$, then the acoustic pressure field at \mathbf{x}_A is given by $p(\mathbf{x}_A, \mathbf{x}, t) = G(\mathbf{x}_A, \mathbf{x}, t) * s(t)$. A similar expression holds for the field at \mathbf{x}_B . Convolving both sides of equation (36) with the autocorrelation $C_s(t)$ of the source wavelet $s(t)$, i.e., $C_s(t) = s(t) * s(-t)$, we obtain

$$G_h(\mathbf{x}_B, \mathbf{x}_A, t) * C_s(t) \approx \frac{2}{\rho_0 c_0} \oint_{\partial\mathbb{D}} p(\mathbf{x}_B, \mathbf{x}, t) * p(\mathbf{x}_A, \mathbf{x}, -t) d^2\mathbf{x}. \quad (38)$$

This expression underlies seismic interferometry with controlled-source data (Bakulin and Calvert 2006; Schuster 2009). For the derivation of ambient-noise interferometry, we consider the situation in which the sources at all \mathbf{x} on $\partial\mathbb{D}$ are simultaneously acting noise sources $N(\mathbf{x}, t)$. In this case, the fields at \mathbf{x}_A and \mathbf{x}_B are given by $p(\mathbf{x}_A, t) = \oint_{\partial\mathbb{D}} G(\mathbf{x}_A, \mathbf{x}, t) * N(\mathbf{x}, t) d^2\mathbf{x}$ and $p(\mathbf{x}_B, t) = \oint_{\partial\mathbb{D}} G(\mathbf{x}_B, \mathbf{x}, t) * N(\mathbf{x}, t) d^2\mathbf{x}$, respectively. We assume that the noise sources are mutually uncorrelated, according to $\langle N(\mathbf{x}', t) * N(\mathbf{x}, -t) \rangle = \delta(\mathbf{x} - \mathbf{x}') C_N(t)$. Here, $C_N(t)$ is the autocorrelation of the noise (which is assumed to be the same for all sources) and $\langle \cdot \rangle$ stands for time averaging. Furthermore, $\delta(\mathbf{x} - \mathbf{x}')$ is a 2D delta function defined in $\partial\mathbb{D}$. The cross correlation of the fields at \mathbf{x}_A and \mathbf{x}_B thus gives

$$\begin{aligned} & \langle p(\mathbf{x}_B, t) * p(\mathbf{x}_A, -t) \rangle \\ &= \left\langle \oint_{\partial\mathbb{D}} \oint_{\partial\mathbb{D}} G(\mathbf{x}_B, \mathbf{x}', t) * N(\mathbf{x}', t) * G(\mathbf{x}_A, \mathbf{x}, -t) \right. \\ & \quad \left. * N(\mathbf{x}, -t) d^2\mathbf{x} d^2\mathbf{x}' \right\rangle \\ &= \oint_{\partial\mathbb{D}} G(\mathbf{x}_B, \mathbf{x}, t) * G(\mathbf{x}_A, \mathbf{x}, -t) * C_N(t) d^2\mathbf{x}. \end{aligned} \quad (39)$$

Figure 8 Illustration of seismic interferometry, for the 2D inhomogeneous medium of Fig. 1. Both panels show the retrieved response $G_h(\mathbf{x}_B, \mathbf{x}_A, t) * C_s(t)$ for a virtual source at \mathbf{x}_A indicated by the red dot in Fig. 1(a), receivers at variable \mathbf{x}_B at the same depth level as the virtual source, and variable time $t \geq 0$. (a) Result obtained when primary sources enclose the medium. (b) *Idem*, when primary sources are confined to the upper boundary.



Convolving both sides of equation (36) with the autocorrelation $C_N(t)$ and using equation (39) to simplify the right-hand side, we obtain

$$G_h(\mathbf{x}_B, \mathbf{x}_A, t) * C_N(t) \approx \frac{2}{\rho_0 c_0} \langle p(\mathbf{x}_B, t) * p(\mathbf{x}_A, -t) \rangle. \quad (40)$$

This is the basic expression for ambient-noise interferometry (Weaver and Lobkis 2001; Wapenaar *et al.* 2002, 2005; Derode *et al.* 2003b; Campillo and Paul 2003; Snieder 2004). It states that the cross correlation of two noise observations at \mathbf{x}_A and \mathbf{x}_B , averaged over long-enough time, converges to the homogeneous Green's function, convolved with the autocorrelation of the noise.

Numerical examples

Based on the analogy between the time-reversal expressions (equations (8) and (9)) and the interferometric expressions (equations (38) and (40)), the numerical examples discussed

for the time-reversal method apply, with some minor modifications, also for seismic interferometry. For example, consider Fig. 3. The response $v_n(\mathbf{x}, \mathbf{x}_A, t) \approx p(\mathbf{x}, \mathbf{x}_A, t)/\rho_0 c_0$ in Fig. 3(a) can, by reciprocity and scaling, be interpreted as $p(\mathbf{x}_A, \mathbf{x}, t)$, i.e., the pressure observed by a single receiver at \mathbf{x}_A due to sources at all \mathbf{x} on the enclosing boundary. Assuming that similar responses are available for other receiver positions \mathbf{x}_B , then cross correlation and integration along the source coordinate, as expressed by the right-hand side of equation (38), yield $G_h(\mathbf{x}_B, \mathbf{x}_A, t) * C_s(t)$. This is shown by the snapshots in Fig. 3(b)–(e), except that, in those figures, the wavelet $s(-t)$ should be replaced by the autocorrelation $C_s(t)$ (note that $s(t)$ is a Ricker wavelet, which is symmetric, like the autocorrelation $C_s(t)$).

In seismic interferometry, it is more common to evaluate space–time panels (i.e., virtual-source gathers) rather than snapshots at constant time. Figure 8(a) shows $G_h(\mathbf{x}_B, \mathbf{x}_A, t) * C_s(t)$ for a fixed virtual-source position $\mathbf{x}_A = (0, 800)$ m,

variable receiver positions $\mathbf{x}_B = (x_1, x_3 = 800)$ m, and variable time $t \geq 0$. Note that this is the same field, as shown in Fig. 3(b)–(e), but represented in a different way. For example, the cross section in Fig. 8(a) at $t = 0.15$ seconds is identical to the cross section in Fig. 3(e) at $x_3 = 800$ m.

When the sources are available only on a single boundary, then similar artefacts occur as in the time-reversal method. Figure 8(b) shows the seismic interferometry result for the situation that the sources are confined to the upper boundary. This figure represents the field in Fig. 4 in a different way: the cross section in Fig. 8(b) at $t = 0.15$ seconds is identical to the cross section at $x_3 = 800$ m in Fig. 4(d).

The second example (Fig. 8(b)) shows that seismic interferometry does not properly account for backward multiple scattering when the medium is accessible from one side only. It has been argued that artefacts like those in Fig. 8(b) can be significantly reduced when the downgoing part of the field at \mathbf{x}_A is correlated with the upgoing part of the field at \mathbf{x}_B (Mehta *et al.* 2007). A comparable improvement is achieved when the direct field at \mathbf{x}_A is correlated with the scattered field at \mathbf{x}_B (Vasconcelos, Snieder and Douma 2009). Halliday *et al.* (2010) use the latter approach to estimate and suppress scattered surface waves. Other improvements can be obtained by directional balancing (Curtis and Halliday 2010) or by deconvolving (instead of correlating) the upgoing field by the downgoing field, either as a trace-by-trace deconvolution process (Vasconcelos and Snieder 2008a, b) or as a multi-dimensional deconvolution process (Wapenaar, Slob and Snieder 2008; van der Neut *et al.* 2011). Another interferometric method that handles multiple scattering well (at least in theory) is passive body-wave interferometry. In this case, primary sources in the subsurface illuminate the medium only from below. However, since the Earth's surface is a free surface, no sources are required at the surface to close the source boundary (another interpretation is that the waves reflected by the free surface account for the illumination from above). Hence, the Green's function retrieved by passive body-wave interferometry properly includes (backward and forward) multiply-scattered waves. This has been derived for horizontally layered media by Claerbout (1968) and has later been generalised for 3D media (Wapenaar 2004).

Analysis of the virtual source

The virtual source obtained by seismic interferometry is defined as the space- and time-dependent field and its derivative, evaluated at $t = 0$; hence, in the ideal case,

$$V(\mathbf{x}, \mathbf{x}_A) = [G_h(\mathbf{x}, \mathbf{x}_A, t) * C(t)]_{t=0}, \quad (41)$$

$$\dot{V}(\mathbf{x}, \mathbf{x}_A) = \left[\frac{\partial}{\partial t} \{G_h(\mathbf{x}, \mathbf{x}_A, t) * C(t)\} \right]_{t=0}, \quad (42)$$

where $C(t)$ can stand for the autocorrelation $C_s(t)$ of the source wavelet $s(t)$ in the case of controlled-source interferometry (equation (38)) or for the autocorrelation $C_N(t)$ of the noise in the case of ambient-noise interferometry (equation (40)). Note that expressions (41) and (42) are nearly identical to those for time-reversal acoustics (equations (10) and (12)). The only difference is that the time-reversed source wavelet $s(-t)$ in equations (10) and (12) is replaced by the autocorrelation $C(t)$ in equations (41) and (42). The autocorrelation is, by definition, symmetric. Hence, all previously obtained expressions for V and \dot{V} containing the symmetric source wavelet $s_{\text{sym}}(t)$ describe the virtual source obtained by seismic interferometry when $s_{\text{sym}}(t)$ is replaced by $C(t)$. In particular, Figs. 3(d) and 5(b), analytically described by equation (20) (with $\dot{s}_{\text{sym}}(t)$ replaced by $\dot{C}(t)$), represent the virtual source for the interferometric response in Fig. 8(a).

DISCUSSION

Time-reversal acoustics and seismic interferometry have many applications in seismology, including exploration seismics. Unlike in ultrasonic time reversal (Fink 1997), physically emitting a time-reversed field into the earth by means of a phased array is impracticable. The best known application of time-reversal acoustics in exploration seismics is model-driven reverse-time migration (Hemon 1978; Whitmore 1983; McMechan 1983), which nowadays is one of the standard methods for depth imaging (Etgen, Gray and Zhang 2009; Zhang and Sun 2009; Clapp, Fu and Lindtjorn 2010; Liu *et al.* 2011; Jones 2014). Another important seismic application of time-reversal acoustics is source characterisation (McMechan 1982; Gajewski and Tessmer 2005; Larmat, Guyer and Johnson 2010). In each of these seismic time-reversal methods, a time-reversed wave field is numerically emitted from one side into a model of the medium. These methods are successful as long as multiple scattering (forward or backward) can be ignored.

Seismic interferometry is widely applied in regional seismology for tomographic surface-wave inversion using ambient noise (Shapiro *et al.* 2005; Sabra *et al.* 2005; Lin, Ritzwoller and Snieder 2009; Boschi and Weemstra 2015). In exploration seismics, it is used for body-wave reflection imaging using controlled-source data (Bakulin and Calvert 2006; Schuster 2009) or ambient noise (Draganov *et al.* 2009; Ryberg 2011). Seismic interferometry is a data-driven method

that does not make use of a model of the medium. Similar as single-sided ultrasonic time reversal, single-sided seismic interferometry accounts for forward multiple scattering. Hence, single-sided seismic interferometry is successful as long as backward multiple scattering does not play a significant role.

One of the aims of this paper is the analysis of time-reversal acoustics and seismic interferometry for situations in which the effects of multiple scattering are not negligible. The analytically derived virtual-source functions and their responses (the homogeneous Green's functions) apply to the ideal situation in which all multiple scattering is taken into account. This requires access to the medium from all sides; see Figs. 3, 5(b), and 8(a). In most practical situations, the medium is accessible from one side only. As a consequence, the retrieved virtual source radiates mainly in one direction and the virtual-source functions and their responses are contaminated by artefacts due to erroneously handled multiple reflections; see Figs. 4, 5(c), and 8(b). The data-driven single-sided focusing approach discussed in Part II aims at circumventing these shortcomings. To this end, we approach focusing as an inverse filtering process rather than a time-reversal process. We show that the focusing functions for single-sided focusing can be retrieved from single-sided reflection data. Using this approach, we obtain virtual-source functions and responses that closely resemble those obtained in this paper for the ideal situation in which the medium can be accessed from all sides.

CONCLUSIONS

By emitting a focusing wave field (physically or synthetically) from the boundary of a medium into that medium, a focused field is obtained at $t = 0$, which acts as a virtual source for the field at $t > 0$. The properties of the focal spot, and hence of the virtual source, depend strongly on the properties of the focusing wave field and the conditions under which this field is emitted into the medium. In this paper, we have defined focusing wave fields as the time reversal of observed fields. A time-reversed point-source response, when emitted into the medium from the enclosing boundary, collapses to an isotropic focus, which, in turn, acts as an isotropic virtual source. This virtual source acts as an initial condition at $t = 0$ for the field at $t > 0$. Although it has a finite spatial resolution, its response for $t > t_s$ (where t_s is half the duration of the wavelet) is, at least in theory, indistinguishable from the response to a true point source.


When the time-reversed point-source response is emitted into the medium from an open boundary, the virtual source is far from isotropic (for example, when the focal point is

illuminated mainly from above, the virtual source radiates mainly downward). Moreover, multiple scattering (in particular backward scattering) gives rise to significant artefacts. The data-driven single-sided focusing approach discussed in Part II aims at circumventing these shortcomings.

ACKNOWLEDGEMENTS

The authors would like to thank the anonymous reviewers and associate editor Colin Thomson for their constructive comments, which helped us improve the paper.

ORCID

Kees Wapenaar  <http://orcid.org/0000-0002-1620-8282>

REFERENCES

- Bakulin A. and Calvert R. 2006. The virtual source method: Theory and case study. *Geophysics* **71**(4), SI139–SI150.
- Berkhout A.J. 1984. *Seismic Migration. Imaging of Acoustic Energy by Wave Field Extrapolation: B. Practical Aspects*. Elsevier.
- Berkhout A.J. and Wapenaar C.P.A. 1993. A unified approach to acoustical reflection imaging. Part II: The inverse problem. *Journal of the Acoustical Society of America* **93**(4), 2017–2023.
- Berryhill J.R. 1984. Wave-equation datuming before stack. *Geophysics* **49**, 2064–2066.
- Bojarski N.N. 1983. Generalized reaction principles and reciprocity theorems for the wave equations, and the relationship between the time-advanced and time-retarded fields. *Journal of the Acoustical Society of America* **74**, 281–285.
- Boschi L. and Weemstra C. 2015. Stationary-phase integrals in the cross correlation of ambient noise. *Reviews of Geophysics* **53**, 411–451.
- Broggini F. and Snieder R. 2012. Connection of scattering principles: a visual and mathematical tour. *European Journal of Physics* **33**, 593–613.
- Campillo M. and Paul A. 2003. Long-range correlations in the diffuse seismic coda. *Science* **299**, 547–549.
- Claerbout J.F. 1968. Synthesis of a layered medium from its acoustic transmission response. *Geophysics* **33**, 264–269.
- Clapp R.G., Fu H. and Lindtjorn O. 2010. Selecting the right hardware for reverse time migration. *The Leading Edge* **29**, 48–58.
- Coulouvrat F. 1993. Continuous field radiated by a geometrically focused transducer: numerical investigation and comparison with an approximate model. *Journal of the Acoustical Society of America* **94**(3), 1663–1675.
- Curtis A. and Halliday D. 2010. Directional balancing for seismic and general wavefield interferometry. *Geophysics* **75**(1), SA1–SA14.
- Curtis A., Nicolson H., Halliday D., Trampert J. and Baptie B. 2009. Virtual seismometers in the subsurface of the Earth from seismic interferometry. *Nature Geoscience* **2**, 700–704.
- de Hoop A.T. 1988. Time-domain reciprocity theorems for acoustic wave fields in fluids with relaxation. *Journal of the Acoustical Society of America* **84**, 1877–1882.

- Derode A., Larose E., Campillo M. and Fink M. 2003. How to estimate the Green's function of a heterogeneous medium between two passive sensors? Application to acoustic waves. *Applied Physics Letters* 83(15), 3054–3056.
- Derode A., Larose E., Tanter M., de Rosny J., Tourin A., Campillo M. *et al.* 2003. Recovering the Green's function from field-field correlations in an open scattering medium (L). *Journal of the Acoustical Society of America* 113(6), 2973–2976.
- Douma J. and Snieder R. 2015. Focusing of elastic waves for microseismic imaging. *Geophysical Journal International* 200, 390–401.
- Draganov D., Campman X., Thorbecke J., Verdel A. and Wapenaar K. 2009. Reflection images from ambient seismic noise. *Geophysics* 74(5), A63–A67.
- Drinkwater B.W. and Wilcox P.D. 2006. Ultrasonic arrays for non-destructive evaluation: a review. *NDT & E International* 39(7), 525–541.
- Esmeys C. and Oristaglio M. 1988. Reverse-time wave-field extrapolation, imaging, and inversion. *Geophysics* 53, 920–931.
- Etgen J., Gray S.H. and Zhang Y. 2009. An overview of depth imaging in exploration geophysics. *Geophysics* 74(6), WCA5–WCA17.
- Fink M. 1997. Time reversed acoustics. *Physics Today* 50, 34–40.
- Fink M. and Prada C. 2001. Acoustic time-reversal mirrors. *Inverse Problems* 17, R1–R38.
- Fokkema J.T. and van den Berg P.M. 1993. *Seismic Applications of Acoustic Reciprocity*. Amsterdam, The Netherlands: Elsevier.
- Gajewski D. and Tessmer E. 2005. Reverse modelling for seismic event characterization. *Geophysical Journal International* 163, 276–284.
- Gouédar P., Stehly L., Brenguier F., Campillo M., Colin de Verdière Y., Larose E. *et al.* 2008. Cross-correlation of random fields: mathematical approach and applications. *Geophysical Prospecting* 56, 375–393.
- Halliday D.F., Curtis A., Vermeer P., Strobba C., Glushchenko A., van Manen D.-J. *et al.* 2010. Interferometric ground-roll removal: attenuation of scattered surface waves in single-sensor data. *Geophysics* 75(2), SA15–SA25.
- Hemon Ch. 1978. Equations d'onde et modes. *Geophysical Prospecting* 26, 790–821.
- Jones I.F. 2014. Tutorial: migration imaging conditions. *First Break* 32(12), 45–55.
- Langenberg K.J., Berger M., Kreutter T., Mayer K. and Schmitz V. 1986. Synthetic aperture focusing technique signal processing. *NDT International* 19(3), 177–189.
- Larmat C., Guyer R.A. and Johnson P.A. 2010. Time-reversal methods in geophysics. *Physics Today* 63(8), 31–35.
- Lerosey G., de Rosny J., Tourin A. and Fink M. 2007. Focusing beyond the diffraction limit with far-field time reversal. *Science* 315, 1120–1122.
- Lin F.-C., Ritzwoller M.H. and Snieder R. 2009. Eikonal tomography: surface wave tomography by phase front tracking across a regional broad-band seismic array. *Geophysical Journal International* 177, 1091–1110.
- Liu F., Zhang G., Morton S.A. and Leveille J.P. 2011. An effective imaging condition for reverse-time migration using wavefield decomposition. *Geophysics* 76, S29–S39.
- Madsen E.L., Goodsitt M.M. and Zagzebski J.A. 1981. Continuous waves generated by focused radiators. *Journal of the Acoustical Society of America* 70(5), 1508–1517.
- McMechan G.A. 1982. Determination of source parameters by wave-field extrapolation. *Geophysical Journal of the Royal Astronomical Society* 71, 613–628.
- McMechan G.A. 1983. Migration by extrapolation of time-dependent boundary values. *Geophysical Prospecting* 31, 413–420.
- Mehta K., Bakulin A., Sheiman J., Calvert R. and Snieder R. 2007. Improving the virtual source method by wavefield separation. *Geophysics* 72(4), V79–V86.
- Oristaglio M.L. 1989. An inverse scattering formula that uses all the data. *Inverse Problems* 5, 1097–1105.
- Porter R.P. 1970. Diffraction-limited, scalar image formation with holograms of arbitrary shape. *Journal of the Optical Society of America* 60, 1051–1059.
- Ryberg T. 2011. Body wave observations from cross-correlations of ambient seismic noise: a case study from the Karoo, RSA. *Geophysical Research Letters* 38, L13311.
- Sabra K.G., Gerstoft P., Roux P., Kuperman W.A. and Fehler M.C. 2005. Surface wave tomography from microseisms in Southern California. *Geophysical Research Letters* 32, L14311.
- Schuster G.T. 2001. Theory of daylight/interferometric imaging: tutorial. 63rd EAGE annual international meeting, Extended Abstracts, A32.
- Schuster G.T. 2009. *Seismic Interferometry*. Cambridge University Press.
- Shapiro N.M., Campillo M., Stehly L. and Ritzwoller M.H. 2005. High-resolution surface-wave tomography from ambient seismic noise. *Science* 307, 1615–1618.
- Snieder R. 2004. Extracting the Green's function from the correlation of coda waves: a derivation based on stationary phase. *Physical Review E* 69, 046610.
- Snieder R., Miyazawa M., Slob E., Vasconcelos I. and Wapenaar K. 2009. A comparison of strategies for seismic interferometry. *Surveys in Geophysics* 30, 503–523.
- van der Neut J., Thorbecke J., Mehta K., Slob E. and Wapenaar K. 2011. Controlled-source interferometric redatuming by cross-correlation and multidimensional deconvolution in elastic media. *Geophysics* 76(4), SA63–SA76.
- van der Neut J., Wapenaar K., Thorbecke J., Slob E. and Vasconcelos I. 2015. An illustration of adaptive Marchenko imaging. *The Leading Edge* 34, 818–822.
- van Manen D.-J., Robertsson J.O.A. and Curtis A. 2005. Modeling of wave propagation in inhomogeneous media. *Physical Review Letters* 94, 164301.
- Vasconcelos I. and Snieder R. 2008a. Interferometry by deconvolution: Part 1—Theory for acoustic waves and numerical examples. *Geophysics* 73(3), S115–S128.
- Vasconcelos I. and Snieder R. 2008b. Interferometry by deconvolution: Part 2—Theory for elastic waves and application to drill-bit seismic imaging. *Geophysics* 73(3), S129–S141.
- Vasconcelos I., Snieder R. and Douma H. 2009. Representation theorems and Green's function retrieval for scattering in acoustic media. *Physical Review E* 80, 036605.

- Wapenaar K. 2004. Retrieving the elastodynamic Green's function of an arbitrary inhomogeneous medium by cross correlation. *Physical Review Letters* **93**, 254301.
- Wapenaar K., Draganov D., Thorbecke J. and Fokkema J. 2002. Theory of acoustic daylight imaging revisited. 72nd SEG annual international meeting, Expanded Abstracts, 2269–2272.
- Wapenaar K., Fokkema J. and Snieder R. 2005. Retrieving the Green's function in an open system by cross-correlation: a comparison of approaches (L). *Journal of the Acoustical Society of America* **118**, 2783–2786.
- Wapenaar K., Slob E. and Snieder R. 2008. Seismic and electromagnetic controlled-source interferometry in dissipative media. *Geophysical Prospecting* **56**, 419–434.
- Wapenaar K., Draganov D., Snieder R., Campman X. and Verdel A. 2010. Tutorial on seismic interferometry: Part 1—Basic principles and applications. *Geophysics* **75**(5), 75A195–75A209.
- Wapenaar K., van der Neut J., Ruigrok E., Draganov D., Hunziker J., Slob E. *et al.* 2011. Seismic interferometry by crosscorrelation and by multidimensional deconvolution: a systematic comparison. *Geophysical Journal International* **185**, 1335–1364.
- Wapenaar K., Thorbecke J., van der Neut J., Brogini F., Slob E. and Snieder R. 2014. Marchenko imaging. *Geophysics* **79**(3), WA39–WA57.
- Weaver R.L. and Lobkis O.I. 2001. Ultrasonics without a source: thermal fluctuation correlations at MHz frequencies. *Physical Review Letters* **87**, 134301.
- Whitmore N.D. 1983. Iterative depth migration by backward time propagation. 53rd SEG annual international meeting, Expanded Abstracts, 382–385.
- Zhang Y. and Sun J. 2009. Practical issues in reverse time migration: true amplitude gathers, noise removal and harmonic source encoding. *First Break* **27**(1), 53–59.

APPENDIX A: CLASSICAL REPRESENTATION OF THE HOMOGENEOUS GREEN'S FUNCTION

Definition of the homogeneous Green's function

Consider an inhomogeneous lossless acoustic medium with compressibility $\kappa(\mathbf{x})$ and mass density $\rho(\mathbf{x})$. In this medium, a source distribution $q(\mathbf{x}, t)$ is present, defined as the volume-injection rate density. The acoustic wave field, caused by this source distribution, is described in terms of the acoustic pressure $p(\mathbf{x}, t)$ and the particle velocity $v_i(\mathbf{x}, t)$. These field quantities obey the equation of motion and the stress–strain relation defined as

$$\rho \partial_t v_i + \partial_i p = 0 \quad (\text{A-1})$$

and

$$\kappa \partial_t p + \partial_i v_i = q, \quad (\text{A-2})$$

respectively. Here, ∂_t and ∂_i stand for the temporal and spatial differential operators $\partial/\partial t$ and $\partial/\partial x_i$, respectively. When q is an impulsive source at $\mathbf{x} = \mathbf{x}_A$ and $t = 0$, according to

$$q(\mathbf{x}, t) = \delta(\mathbf{x} - \mathbf{x}_A) \delta(t), \quad (\text{A-3})$$

then the causal solution of equations (A-1) and (A-2) defines the Green's function, according to

$$p(\mathbf{x}, t) = G(\mathbf{x}, \mathbf{x}_A, t). \quad (\text{A-4})$$

By eliminating v_i from equations (A-1) and (A-2) and substituting equations (A-3) and (A-4), we find that the Green's function $G(\mathbf{x}, \mathbf{x}_A, t)$ obeys the following wave equation:

$$\partial_i (\rho^{-1} \partial_i G) - \kappa \partial_t^2 G = -\delta(\mathbf{x} - \mathbf{x}_A) \delta(t). \quad (\text{A-5})$$

We introduce a second type of Green's function that obeys the same wave equation and causality condition but with the derivative of the delta function replaced by the delta function according to

$$\partial_i (\rho^{-1} \partial_i \mathcal{G}) - \kappa \partial_t^2 \mathcal{G} = -\delta(\mathbf{x} - \mathbf{x}_A) \delta(t). \quad (\text{A-6})$$

By differentiating both sides of equation (A-6) with respect to t and comparing the resulting equation with equation (A-5), it follows that G and \mathcal{G} are related via

$$G(\mathbf{x}, \mathbf{x}_A, t) = \partial_t \mathcal{G}(\mathbf{x}, \mathbf{x}_A, t). \quad (\text{A-7})$$

Because wave equation (A-6) is symmetric in time, the time-reversed Green's function $\mathcal{G}(\mathbf{x}, \mathbf{x}_A, -t)$ obeys the same wave equation with the same source. By subtracting the wave equations for $\mathcal{G}(\mathbf{x}, \mathbf{x}_A, t)$ and $\mathcal{G}(\mathbf{x}, \mathbf{x}_A, -t)$, the sources on the right-hand sides cancel each other; hence, the difference function

$$\mathcal{G}_h(\mathbf{x}, \mathbf{x}_A, t) = \mathcal{G}(\mathbf{x}, \mathbf{x}_A, t) - \mathcal{G}(\mathbf{x}, \mathbf{x}_A, -t) \quad (\text{A-8})$$

obeys the homogeneous equation

$$\partial_i (\rho^{-1} \partial_i \mathcal{G}_h) - \kappa \partial_t^2 \mathcal{G}_h = 0. \quad (\text{A-9})$$

Therefore, $\mathcal{G}_h(\mathbf{x}, \mathbf{x}_A, t)$, as defined in equation (A-8), is called the homogeneous Green's function.

Wave equation (A-5) is also symmetric in time, except for the source on the right-hand side, which is anti-symmetric. Hence, the time-reversed Green's function $G(\mathbf{x}, \mathbf{x}_A, -t)$ obeys the same wave equation but with opposite sign for the source. By summing the wave equations for $G(\mathbf{x}, \mathbf{x}_A, t)$ and $G(\mathbf{x}, \mathbf{x}_A, -t)$, the sources on the right-hand sides cancel each other; hence, the function

$$G_h(\mathbf{x}, \mathbf{x}_A, t) = G(\mathbf{x}, \mathbf{x}_A, t) + G(\mathbf{x}, \mathbf{x}_A, -t) \quad (\text{A-10})$$

obeys the homogeneous equation

$$\partial_i (\rho^{-1} \partial_i G_h) - \kappa \partial_i^2 G_h = 0. \quad (\text{A-11})$$

Here, $G_h(\mathbf{x}, \mathbf{x}_A, t)$ is also a homogeneous Green's function.

From equations (A-7), (A-8), and (A-10), it follows that G_h and \mathcal{G}_h are related via

$$G_h(\mathbf{x}, \mathbf{x}_A, t) = \partial_i \mathcal{G}_h(\mathbf{x}, \mathbf{x}_A, t). \quad (\text{A-12})$$

Reciprocity theorems

We define the temporal Fourier transform of a space- and time-dependent quantity $p(\mathbf{x}, t)$ as

$$p(\mathbf{x}, \omega) = \int_{-\infty}^{\infty} p(\mathbf{x}, t) \exp(-j\omega t) dt, \quad (\text{A-13})$$

where ω is the angular frequency and j is the imaginary unit. To keep the notation simple, we denote quantities in the time and frequency domain by the same symbol. In the frequency domain, equations (A-1) and (A-2) transform to

$$j\omega \rho v_i + \partial_i p = 0 \quad (\text{A-14})$$

and

$$j\omega \kappa p + \partial_i v_i = q, \quad (\text{A-15})$$

respectively. We introduce two independent acoustic states, which will be distinguished by subscripts A and B . Rayleigh's reciprocity theorem is obtained by considering the quantity $\partial_i \{p_A v_{i,B} - v_{i,A} p_B\}$, applying the product rule for differentiation, substituting equations (A-14) and (A-15) for both states, integrating the result over a spatial domain \mathbb{D} enclosed by boundary $\partial\mathbb{D}$ with outward pointing normal n_i , and applying the theorem of Gauss (de Hoop 1988; Fokkema and van den Berg 1993). This yields Rayleigh's reciprocity theorem of the convolution type

$$\int_{\mathbb{D}} \{p_A q_B - q_A p_B\} d^3\mathbf{x} = \oint_{\partial\mathbb{D}} \{p_A v_{i,B} - v_{i,A} p_B\} n_i d^2\mathbf{x}. \quad (\text{A-16})$$

We assumed that, in \mathbb{D} , the medium parameters $\kappa(\mathbf{x})$ and $\rho(\mathbf{x})$ in the two states are identical. We derive a second form of Rayleigh's reciprocity theorem for time-reversed wave fields. In the frequency domain, time reversal is replaced by complex conjugation. When p and v_i are a solution of equations (A-14) and (A-15) with source distribution q (and real-valued medium parameters), then p^* and $-v_i^*$ obey the same equations with source distribution $-q^*$ (superscript $*$ denotes complex conjugation). Making these substitutions for state A in

equation (A-16), we obtain Rayleigh's reciprocity theorem of the correlation type (Bojarski 1983)

$$\int_{\mathbb{D}} \{p_A^* q_B + q_A^* p_B\} d^3\mathbf{x} = \oint_{\partial\mathbb{D}} \{p_A^* v_{i,B} + v_{i,A}^* p_B\} n_i d^2\mathbf{x}. \quad (\text{A-17})$$

Note that, when parts of the boundary $\partial\mathbb{D}$ are either free or fixed in both states, such that either the pressure p or the normal component of the particle velocity $v_i n_i$ vanishes on $\partial\mathbb{D}$, the boundary integrals in equations (A-16) and (A-17) need only be evaluated over the remaining part of the boundary.

Representation of the homogeneous Green's function

We choose point sources in both states, according to $q_A(\mathbf{x}, \omega) = \delta(\mathbf{x} - \mathbf{x}_A)$ and $q_B(\mathbf{x}, \omega) = \delta(\mathbf{x} - \mathbf{x}_B)$, with \mathbf{x}_A and \mathbf{x}_B both in \mathbb{D} . The field in state A is thus expressed in terms of the Green's function, according to

$$p_A(\mathbf{x}, \omega) = G(\mathbf{x}, \mathbf{x}_A, \omega) \quad (\text{A-18})$$

and

$$v_{i,A}(\mathbf{x}, \omega) = -(j\omega \rho(\mathbf{x}))^{-1} \partial_i G(\mathbf{x}, \mathbf{x}_A, \omega), \quad (\text{A-19})$$

with $G(\mathbf{x}, \mathbf{x}_A, \omega)$ being the Fourier transform of $G(\mathbf{x}, \mathbf{x}_A, t)$. Similar expressions hold for the wave field in state B . Making these substitutions in equation (A-17) and using source-receiver reciprocity of the Green's functions gives (Wapenaar 2004; van Manen *et al.* 2005)

$$G_h(\mathbf{x}_B, \mathbf{x}_A, \omega) = \oint_{\partial\mathbb{D}} \frac{-1}{j\omega \rho(\mathbf{x})} \{ \partial_i G(\mathbf{x}_B, \mathbf{x}, \omega) G^*(\mathbf{x}, \mathbf{x}_A, \omega) - G(\mathbf{x}_B, \mathbf{x}, \omega) \partial_i G^*(\mathbf{x}, \mathbf{x}_A, \omega) \} n_i d^2\mathbf{x}, \quad (\text{A-20})$$

where $G_h(\mathbf{x}_B, \mathbf{x}_A, \omega)$ is the homogeneous Green's function in the frequency domain defined as

$$G_h(\mathbf{x}_B, \mathbf{x}_A, \omega) = G(\mathbf{x}_B, \mathbf{x}_A, \omega) + G^*(\mathbf{x}_B, \mathbf{x}_A, \omega) = 2\Re\{G(\mathbf{x}_B, \mathbf{x}_A, \omega)\}, \quad (\text{A-21})$$

where \Re denotes the real part. Equation (A-20) is an exact representation for the homogeneous Green's function $G_h(\mathbf{x}_B, \mathbf{x}_A, \omega)$.

When $\partial\mathbb{D}$ is sufficiently smooth and the medium outside $\partial\mathbb{D}$ is homogeneous (with mass density ρ_0 and compressibility κ_0), the two terms under the integral in equation (A-20) are nearly identical (but with opposite signs); hence

$$G_h(\mathbf{x}_B, \mathbf{x}_A, \omega) \approx \frac{2}{j\omega \rho_0} \oint_{\partial\mathbb{D}} G(\mathbf{x}_B, \mathbf{x}, \omega) \partial_i G^*(\mathbf{x}, \mathbf{x}_A, \omega) n_i d^2\mathbf{x}. \quad (\text{A-22})$$

The main approximation is that evanescent waves are neglected at $\partial\mathbb{D}$ (Wapenaar *et al.* 2011). Taking the inverse Fourier transform of equation (A-22), convolving both sides with a time-reversed wavelet $s(-t)$, and noting that the spatial derivative of the Green's function is proportional to particle velocity, we yield equation (9).

A further simplification of equation (A-22) is possible when $\partial\mathbb{D}$ is a sphere with a very large radius. In this case, we may approximate $\partial_i G(\mathbf{x}, \mathbf{x}_A, \omega) n_i$ on $\partial\mathbb{D}$ by $-j(\omega/c_0)G(\mathbf{x}, \mathbf{x}_A, \omega)$ (Wapenaar *et al.* 2005), with propagation velocity $c_0 = (\kappa_0 \rho_0)^{-1/2}$. Using this approximation in equation (A-22) gives

$$G_h(\mathbf{x}_B, \mathbf{x}_A, \omega) \approx \frac{2}{\rho_0 c_0} \oint_{\partial\mathbb{D}} G(\mathbf{x}_B, \mathbf{x}, \omega) G^*(\mathbf{x}, \mathbf{x}_A, \omega) d^2\mathbf{x}. \quad (\text{A-23})$$

Taking the inverse Fourier transform of equation (A-23) yields equation (3), with proportionality factor $2/\rho_0 c_0$. Convolving both sides with $s(-t)$ gives equation (8).

We define $\mathcal{G}(\mathbf{x}, \mathbf{x}_A, \omega)$ as the Fourier transform of $G(\mathbf{x}, \mathbf{x}_A, t)$. Analogous to equation (A-20), the representation for the homogeneous Green's function $\mathcal{G}_h(\mathbf{x}_B, \mathbf{x}_A, \omega)$ reads

$$\mathcal{G}_h(\mathbf{x}_B, \mathbf{x}_A, \omega) = \oint_{\partial\mathbb{D}} \frac{1}{\rho(\mathbf{x})} \{ \partial_i \mathcal{G}(\mathbf{x}_B, \mathbf{x}, \omega) \mathcal{G}^*(\mathbf{x}, \mathbf{x}_A, \omega) - \mathcal{G}(\mathbf{x}_B, \mathbf{x}, \omega) \partial_i \mathcal{G}^*(\mathbf{x}, \mathbf{x}_A, \omega) \} n_i d^2\mathbf{x}, \quad (\text{A-24})$$

with

$$\begin{aligned} \mathcal{G}_h(\mathbf{x}_B, \mathbf{x}_A, \omega) &= \mathcal{G}(\mathbf{x}_B, \mathbf{x}_A, \omega) - \mathcal{G}^*(\mathbf{x}_B, \mathbf{x}_A, \omega) \\ &= 2j\Im\{\mathcal{G}(\mathbf{x}_B, \mathbf{x}_A, \omega)\}, \end{aligned} \quad (\text{A-25})$$

where \Im denotes the imaginary part. Equation (A-24) is the homogeneous Green's function representation that was introduced by Porter (1970) for holographic imaging and used by Oristaglio (1989) as the basis for an inverse scattering formulation. Under the same assumptions as above, we may approximate equation (A-24) by

$$\mathcal{G}_h(\mathbf{x}_B, \mathbf{x}_A, \omega) \approx -\frac{2j\omega}{\rho_0 c_0} \oint_{\partial\mathbb{D}} \mathcal{G}(\mathbf{x}_B, \mathbf{x}, \omega) \mathcal{G}^*(\mathbf{x}, \mathbf{x}_A, \omega) d^2\mathbf{x}. \quad (\text{A-26})$$

Taking the inverse Fourier transform yields equation (6), with proportionality factor $2/\rho_0 c_0$.

APPENDIX B: VIRTUAL-SOURCE FUNCTIONS

We analyse the virtual-source functions $V(\mathbf{x}, \mathbf{x}_A)$ and $\dot{V}(\mathbf{x}, \mathbf{x}_A)$ defined by equations (10) and (12), assuming a homogeneous region around the virtual-source position \mathbf{x}_A . Using a more

precise notation, equations (10) and (12) read

$$\begin{aligned} V(\mathbf{x}, \mathbf{x}_A) &= [G_h(\mathbf{x}, \mathbf{x}_A, t) * s(-t)]_{t=0} \\ &= \left[\int_{-\infty}^{\infty} \{G(\mathbf{x}, \mathbf{x}_A, t') + G(\mathbf{x}, \mathbf{x}_A, -t')\} s(t' - t) dt' \right]_{t=0} \end{aligned} \quad (\text{B-1})$$

and

$$\begin{aligned} \dot{V}(\mathbf{x}, \mathbf{x}_A) &= [\partial_t \{G_h(\mathbf{x}, \mathbf{x}_A, t) * s(-t)\}]_{t=0} \\ &= \left[- \int_{-\infty}^{\infty} \{G(\mathbf{x}, \mathbf{x}_A, t') + G(\mathbf{x}, \mathbf{x}_A, -t')\} \dot{s}(t' - t) dt' \right]_{t=0}, \end{aligned} \quad (\text{B-2})$$

respectively, where $\dot{s}(t)$ denotes the first-order derivative of the source wavelet $s(t)$. The Green's function $G(\mathbf{x}, \mathbf{x}_A, t)$ obeys wave equation (A-5). For a homogeneous region around \mathbf{x}_A , with mass density $\bar{\rho}$ and compressibility $\bar{\kappa}$, this wave equation can be written as

$$\partial_i \partial_i G - \bar{\kappa} \bar{\rho} \partial_t^2 G = -\bar{\rho} \delta(\mathbf{x} - \mathbf{x}_A) \partial_t \delta(t). \quad (\text{B-3})$$

In the 3D situation, the causal solution for sufficiently small t (i.e., before the field leaves the homogeneous region) is given by

$$G_{3D}(\mathbf{x}, \mathbf{x}_A, t) = \bar{\rho} \frac{\partial}{\partial t} \frac{\delta(t - r/\bar{c})}{4\pi r}, \quad (\text{B-4})$$

with $r = |\mathbf{x} - \mathbf{x}_A|$ and $\bar{c} = (\bar{\kappa} \bar{\rho})^{-1/2}$. Substituting this into equation (B-1), using integration by parts to move the time derivative from the delta function to the source wavelet, yields

$$\begin{aligned} V_{3D}(\mathbf{x}, \mathbf{x}_A) &= -\frac{\bar{\rho}}{4\pi r} [\{\dot{s}(r/\bar{c} - t) - \dot{s}(-r/\bar{c} - t)\}]_{t=0} \\ &= -\frac{\bar{\rho}}{4\pi r} \{\dot{s}(r/\bar{c}) - \dot{s}(-r/\bar{c})\}. \end{aligned} \quad (\text{B-5})$$

The limit for $\mathbf{x} \rightarrow \mathbf{x}_A$ follows from

$$\begin{aligned} \lim_{\mathbf{x} \rightarrow \mathbf{x}_A} V_{3D}(\mathbf{x}, \mathbf{x}_A) &= -\frac{\bar{\rho}}{2\pi \bar{c}} \lim_{r \rightarrow 0} \frac{\dot{s}(r/\bar{c}) - \dot{s}(-r/\bar{c})}{2r/\bar{c}} \\ &= -\frac{\bar{\rho}}{2\pi \bar{c}} \ddot{s}(0), \end{aligned} \quad (\text{B-6})$$

with $\ddot{s}(t)$ being the second-order derivative of $s(t)$. Similarly, substituting equation (B-4) into equation (B-2) gives

$$\begin{aligned} \dot{V}_{3D}(\mathbf{x}, \mathbf{x}_A) &= \frac{\bar{\rho}}{4\pi r} [\{\ddot{s}(r/\bar{c} - t) - \ddot{s}(-r/\bar{c} - t)\}]_{t=0} \\ &= \frac{\bar{\rho}}{4\pi r} \{\ddot{s}(r/\bar{c}) - \ddot{s}(-r/\bar{c})\}, \end{aligned} \quad (\text{B-7})$$

which has the following limit:

$$\lim_{\mathbf{x} \rightarrow \mathbf{x}_A} \dot{V}_{3D}(\mathbf{x}, \mathbf{x}_A) = \frac{\bar{\rho}}{2\pi\bar{c}} \lim_{r \rightarrow 0} \frac{\ddot{s}(r/\bar{c}) - \ddot{s}(-r/\bar{c})}{2r/\bar{c}} = \frac{\bar{\rho}}{2\pi\bar{c}} \ddot{s}(0), \quad (\text{B-8})$$

with $\ddot{s}(t)$ being the third-order derivative of $s(t)$.

For the 2D situation, the causal solution of equation (B-3) reads

$$G_{2D}(\mathbf{x}, \mathbf{x}_A, t) = \frac{\bar{\rho}}{2\pi} \frac{\partial}{\partial t} \frac{H(t - r/\bar{c})}{\sqrt{t^2 - r^2/\bar{c}^2}}, \quad (\text{B-9})$$

where $H(t)$ is the Heaviside step function. Substituting this into equation (B-1), using integration by parts to move the time derivative to the source wavelet, yields

$$\begin{aligned} V_{2D}(\mathbf{x}, \mathbf{x}_A) &= \left[-\frac{\bar{\rho}}{2\pi} \int_{r/\bar{c}}^{\infty} \frac{\dot{s}(t' - t) - \dot{s}(-t' - t)}{\sqrt{(t')^2 - r^2/\bar{c}^2}} dt' \right]_{t=0} \\ &= -\frac{\bar{\rho}}{2\pi} \int_{r/\bar{c}}^{\infty} \frac{\dot{s}(t') - \dot{s}(-t')}{\sqrt{(t')^2 - r^2/\bar{c}^2}} dt'. \end{aligned} \quad (\text{B-10})$$

Similarly, substituting equation (B-9) into equation (B-2) gives

$$\dot{V}_{2D}(\mathbf{x}, \mathbf{x}_A) = \frac{\bar{\rho}}{2\pi} \int_{r/\bar{c}}^{\infty} \frac{\ddot{s}(t') - \ddot{s}(-t')}{\sqrt{(t')^2 - r^2/\bar{c}^2}} dt'. \quad (\text{B-11})$$

For the 1D situation, the causal solution of equation (B-3) is given by

$$G_{1D}(x_3, x_{3,A}, t) = \frac{\bar{\rho}\bar{c}}{2} \delta(t - r/\bar{c}), \quad (\text{B-12})$$

where $r = |x_3 - x_{3,A}|$. Substituting this into equations (B-1) and (B-2) yields

$$\begin{aligned} V_{1D}(x_3, x_{3,A}) &= \frac{\bar{\rho}\bar{c}}{2} [s(r/\bar{c} - t) + s(-r/\bar{c} - t)]_{t=0} \\ &= \frac{\bar{\rho}\bar{c}}{2} \{s(r/\bar{c}) + s(-r/\bar{c})\} \end{aligned} \quad (\text{B-13})$$

and

$$\begin{aligned} \dot{V}_{1D}(x_3, x_{3,A}) &= -\frac{\bar{\rho}\bar{c}}{2} [\{\dot{s}(r/\bar{c} - t) + \dot{s}(-r/\bar{c} - t)\}]_{t=0} \\ &= -\frac{\bar{\rho}\bar{c}}{2} \{\dot{s}(r/\bar{c}) + \dot{s}(-r/\bar{c})\}, \end{aligned} \quad (\text{B-14})$$

respectively.

Finally, we analyse the virtual-source functions $\mathcal{V}(\mathbf{x}, \mathbf{x}_A)$ and $\dot{\mathcal{V}}(\mathbf{x}, \mathbf{x}_A)$ defined by equations (28) and (29), respectively. The Green's function $\mathcal{G}(\mathbf{x}, \mathbf{x}_A, t)$ obeys wave equation (A-6). For a homogeneous region around \mathbf{x}_A , this wave equation can

be written as

$$\partial_i \partial_i \mathcal{G} - \bar{c} \bar{\rho} \partial_t^2 \mathcal{G} = -\bar{\rho} \delta(\mathbf{x} - \mathbf{x}_A) \delta(t). \quad (\text{B-15})$$

For the 3D situation, the causal solution is given by

$$\mathcal{G}_{3D}(\mathbf{x}, \mathbf{x}_A, t) = \bar{\rho} \frac{\delta(t - r/\bar{c})}{4\pi r}, \quad (\text{B-16})$$

where $r = |\mathbf{x} - \mathbf{x}_A|$. Following the same analysis as above, we find

$$\mathcal{V}_{3D}(\mathbf{x}, \mathbf{x}_A) = \frac{\bar{\rho}}{4\pi r} \{s(r/\bar{c}) - s(-r/\bar{c})\}, \quad (\text{B-17})$$

with limit

$$\lim_{\mathbf{x} \rightarrow \mathbf{x}_A} \mathcal{V}_{3D}(\mathbf{x}, \mathbf{x}_A) = \frac{\bar{\rho}}{2\pi\bar{c}} \dot{s}(0) \quad (\text{B-18})$$

and

$$\dot{\mathcal{V}}_{3D}(\mathbf{x}, \mathbf{x}_A) = -\frac{\bar{\rho}}{4\pi r} \{\dot{s}(r/\bar{c}) - \dot{s}(-r/\bar{c})\}, \quad (\text{B-19})$$

with limit

$$\lim_{\mathbf{x} \rightarrow \mathbf{x}_A} \dot{\mathcal{V}}_{3D}(\mathbf{x}, \mathbf{x}_A) = -\frac{\bar{\rho}}{2\pi\bar{c}} \ddot{s}(0). \quad (\text{B-20})$$

For the 2D situation, the causal solution of equation (B-15) reads

$$\mathcal{G}_{2D}(\mathbf{x}, \mathbf{x}_A, t) = \frac{\bar{\rho}}{2\pi} \frac{H(t - r/\bar{c})}{\sqrt{t^2 - r^2/\bar{c}^2}}. \quad (\text{B-21})$$

With a similar analysis as above, we obtain

$$\mathcal{V}_{2D}(\mathbf{x}, \mathbf{x}_A) = \frac{\bar{\rho}}{2\pi} \int_{r/\bar{c}}^{\infty} \frac{s(t') - s(-t')}{\sqrt{(t')^2 - r^2/\bar{c}^2}} dt' \quad (\text{B-22})$$

and

$$\dot{\mathcal{V}}_{2D}(\mathbf{x}, \mathbf{x}_A) = -\frac{\bar{\rho}}{2\pi} \int_{r/\bar{c}}^{\infty} \frac{\dot{s}(t') - \dot{s}(-t')}{\sqrt{(t')^2 - r^2/\bar{c}^2}} dt'. \quad (\text{B-23})$$

For the 1D situation, the causal solution of equation (B-15) is given by

$$\mathcal{G}_{1D}(x_3, x_{3,A}, t) = \frac{\bar{\rho}\bar{c}}{2} H(t - r/\bar{c}). \quad (\text{B-24})$$

With this function, we obtain

$$\mathcal{V}_{1D}(x_3, x_{3,A}) = -\frac{\bar{\rho}\bar{c}}{2} \{S(r/\bar{c}) + S(-r/\bar{c})\} \quad (\text{B-25})$$

and

$$\dot{\mathcal{V}}_{1D}(x_3, x_{3,A}) = \frac{\bar{\rho}\bar{c}}{2} \{\dot{s}(r/\bar{c}) + \dot{s}(-r/\bar{c})\}, \quad (\text{B-26})$$

with $S(t)$ being the primitive function of $s(t)$.